CONFIRMATION OF AND VARIABLE ENERGY INJECTION BY A NEAR-RELATIVISTIC OUTFLOW IN APM 08279+5255

G. Chartas,[1,2] C. Saez,[2] W. N. Brandt,[2] M. Giustini,[2,3,4] and G. P. Garmire[2]

ABSTRACT

We present results from multi-epoch spectral analysis of *XMM-Newton* and *Chandra* observations of the broad absorption line (BAL) quasar APM 08279+5255. Our analysis shows significant X-ray BALs in all epochs with rest-frame energies lying in the range of ~ 6.7–18 keV. The X-ray BALs and 0.2–10 keV continuum show significant variability on timescales as short as 3.3 days (proper time) implying a source size-scale of $\sim 10\ r_{\rm g}$, where $r_{\rm g}$ is the gravitational radius. We find a large gradient in the outflow velocity of the X-ray absorbers with projected outflow velocities of up to $0.76\ c$. The maximum outflow velocity constrains the angle between the wind velocity and our line of sight to be less than $\sim 22°$. Based on our spectral analysis we identify the following components of the outflow: (a) Highly ionized X-ray absorbing material with an ionization parameter in the range of $2.9 \lesssim \log \xi \lesssim 3.9$ (the units of ξ are erg cm s^{-1}) and a column density of $\log N_{\rm H} \sim 23$ (the units of $N_{\rm H}$ are cm^{-2}) outflowing at velocities of up to $0.76\ c$. (b) Low-ionization X-ray absorbing gas with $\log N_{\rm H} \sim 22.8$. We find a possible trend between the X-ray photon index and the maximum outflow velocity of the ionized absorber in the sense that flatter spectra appear to result in lower outflow velocities. Based on our spectral analysis of observations of APM 08279+5255 over a period of 1.2 years (proper time) we estimate the mass-outflow rate and efficiency of the outflow to have varied between $16^{+12}_{-8}\ M_{\odot}$ yr^{-1} and $64^{+66}_{-40}\ M_{\odot}$ yr^{-1} and $0.18^{+0.15}_{-0.11}$ to $1.7^{+1.9}_{-1.2}$, respectively. Assuming that the outflow properties of APM 08279+5255 are a common property of most quasars at similar redshifts, our results then imply that quasar winds are massive and energetic enough to influence significantly the formation of the host galaxy, provide significant metal enrichment to the interstellar medium (ISM) and intergalactic medium (IGM), and are a viable mechanism for feedback at redshifts near the peak in the number density of galaxy mergers.

Subject headings: galaxies: active — quasars: absorption lines — quasars: individual (APM 08279+5225) — X-rays: galaxies — gravitational lensing

1. INTRODUCTION

A number of physical mechanisms of interactions of AGNs with their environments have been proposed to explain feedback in galaxies and clusters of galaxies. These feedback mechanisms include radio jets, AGN winds, and AGN radiative heating. It may be the case that several of these mechanisms operate simultaneously and their relative contribution to the feedback process varies depending in part on the size of the super-massive black hole (SMBH), and the combined gravitational potential of the SMBH and host galaxy. The gas and dust content of the host galaxy, the redshift and age of the host, and the inflow and outflow properties of the central super-massive black hole may be important as well.

The radio-jet feedback mechanism was proposed after the discovery of significant radio cavities and shock fronts in several clusters of galaxies. The cavity sizes are large enough to imply that the amount of energy injected in the intracluster medium (ICM), as inferred from the mechanical work pdV required to displace the gas in the radio cavities, is sufficient to balance radiative losses, suppress cooling flows, and halt star formation (e.g., Fabian et al. 2009, and references therein). The radio jets are thought to be driven by either accretion onto the black hole (e.g., Blandford & Payne 1982) or the black-hole spin (e.g., Blandford

& Znajek 1977). The details of the process by which radio jets deposit energy and distribute it uniformly throughout the ICM is currently not well understood.

Another possibly important mode that may contribute to feedback is AGN radiation. Radiative heating (e.g., Ciotti & Ostriker 2007) has been proposed as an alternative to the radio-jet mechanism to explain the suppression of cooling flows in isolated elliptical galaxies and possibly in clusters of galaxies.

In field galaxies, especially ones in the redshift range of $z \approx 1 - 3$ where the number density of galaxy mergers is thought to peak (e.g., Di Matteo et al. 2005), quasar winds are thought to be one of the major contributors to feedback. Winds can be driven by radiation pressure, magneto-centrifugal forces, and thermal pressure or a combination of these processes. The potential importance of quasar outflows has been explicitly demonstrated in theoretical models of structure formation and galaxy mergers that incorporate the effects of quasar outflows (e.g., Silk & Rees 1998; Scannapieco & Oh 2004; Granato et al. 2004; Springel, Di Matteo, & Hernquist 2005; Hopkins et al. 2005, 2006). Observational evidence to support these theories of quasar outflows was provided by the discovery of near-relativistic X-ray absorbing winds in several broad absorption line (BAL) quasars (e.g., Chartas et al. 2002, 2003) and later in several non-BAL quasars (e.g., Reeves

[1] Department of Physics and Astronomy, College of Charleston, Charleston, SC, 29424, USA, chartasg@cofc.edu

[2] Department of Astronomy & Astrophysics, Pennsylvania State University, University Park, PA 16802, chartas@astro.psu.edu, saez@astro.psu.edu, niel@astro.psu.edu, giustini@astro.psu.edu, garmire@astro.psu.edu

[3] Dipartimento di Astronomia, Universita degli Studi di Bologna, via Ranzani 1, 40127 Bologna, Italy, margharita.giustini2@iasfbo.inaf.it

[4] INAF/Istituto di Astrofisica Spaziale e Fisica Cosmica di Bologna, via Gobetti 101, 40129 Bologna, Italy, margherita.giustini@unibo.it

et al. 2003; Pounds et al. 2003, 2006; Braito et al. 2007).

The relative contribution of each of these proposed feedback mechanisms will vary in part depending on the following conditions:

(a) The importance of the radio-jet mode will depend on the radio loudness and the duty cycle of the central AGN. The presence of a radio jet in an AGN is likely to depend on the available supply of infalling material to feed the black hole and/or the spin of the black hole. We note that several observations imply that the fraction of radio-loud objects varies with redshift and luminosity (e.g., Peacock et al. 1986; Schneider et al. 1992; La Franca et al. 1994; Jiang et al. 2007). Specifically it is found that the radio-loud fraction decreases with redshift and increases with luminosity. The radio jet mode therefore may be more important at later times and in clusters of galaxies and in nearby massive ellipticals that have a larger probability of containing a radio-loud object compared to galaxies at $z \gtrsim 1$ which are more likely to contain a radio-quiet AGN.

(b) The feedback process is also expected to depend on the mass of the central black hole and the gravitational potential of the host galaxy. In order for a feedback mechanism to be effective it must be able to drive gas out of the host with a velocity that is larger than the escape velocity determined by the gravitational potential of the system. The mass outflow rates and outflow efficiencies of AGN winds will also depend strongly on the mass and luminosity of the SMBH. Analyses of the kinematic properties of UV absorbers in quasars indicate a strong increase in outflow velocity of UV absorbers with quasar UV luminosity (e.g., Laor & Brandt 2002; Ganguly & Brotherton 2008). Luminous quasars are found to contain winds with velocities of the UV outflowing material of up to 60,000 km s^{-1} whereas Seyfert galaxies typically have winds with significantly lower velocities of up to $\sim$ 2,000 km s^{-1}.

(c) Hydrodynamic simulations of AGN atmospheres driven by radiation pressure indicate that the strengths of the outflows originating from AGN accretion disks depend on the Eddington ratio ($L_{\rm Bol}/L_{\rm Edd}$) with more massive and faster winds produced at larger Eddington ratios (e.g., Proga, Stone & Drew 1988; Proga, Stone & Kallman 2000; Proga & Kallman 2004). In systems with a limited supply of gas to fuel the AGN it is expected that AGN winds will be relatively weak.

(d) In the case of a galaxy merger the degree to which each mechanism contributes to the overall feedback process may change with time since the merger event occurred.

Observations in X-rays of the BAL quasar APM 08279+5255, the mini-BAL quasar PG 1115+080, and perhaps the low-ionization BAL quasar H 1413-117 have strongly suggested the presence of near-relativistic outflows of X-ray absorbing material in these objects (Chartas et al. 2002, 2003, 2007a, 2007b). Observations of these quasars in the optical and UV indicate outflow velocities and column densities that are more than an order of magnitude lower than those inferred from the X-ray spectra. These differences in outflow velocities and absorbing column densities suggest that X-ray BALs probe a highly ionized, massive and high-velocity component of the wind

that is largely distinct from the absorbers detected in the optical and UV wavebands. Most of the mass and energy of quasar winds is likely carried by the outflowing X-ray absorbers, and observations in the X-ray band are therefore crucial for improving our understanding of the contribution of quasar winds to feedback in galaxies.

This paper will focus on determining the significance of the wind in the $z = 3.91$ gravitationally lensed BAL quasar APM 08279+5255 in the feedback process during an epoch near the peak of the number density of mergers. Specifically, we present results from analyses of several *XMM-Newton* and *Chandra* observations of APM 08279+5255 in order to determine the outflow velocity and its variability, obtain insights on the acceleration mechanism, constrain the geometry of the wind, and estimate the mass outflow rate and the outflow efficiency.

Throughout this paper we adopt a Λ-dominated cosmology with $H_0 = 70$ km s^{-1} Mpc^{-1}, $\Omega_\Lambda = 0.7$, and $\Omega_{\rm M} = 0.3$.

2. OBSERVATIONS AND DATA ANALYSIS

2.1. *Observations and Data Reduction*

APM 08279+5255 was observed with *XMM-Newton* (Jansen et al. 2001) on 2002 April 28, 2007 October 6, and 2007 October 22, respectively. It was also observed with the Advanced CCD Imaging Spectrometer (ACIS; Garmire et al. 2003) on board the *Chandra X-ray Observatory* (hereafter *Chandra*) on 2002 February 24 and 2008 January 14.

The spectral analysis of the 2002 *Chandra* observation of APM 08279+5255 has been presented in Chartas et al. (2002), and the spectral analysis of the 2002 *XMM-Newton* observation of APM 08279+5255 in Hasinger et al. (2002). Because of recent significant improvements in the calibration of the instruments on board *Chandra* and *XMM-Newton* since the publication of the APM 08279+5255 results, we have re-analyzed all observations. Updates on the calibration of *Chandra* and *XMM-Newton* are reported on the *Chandra* X-ray Center (CXC) and *XMM-Newton* Science Operations Centre (SOC) World Wide Web (WWW) sites, respectively.[5]

We analyzed the *XMM-Newton* data for APM 08279+5255 with the standard analysis software SAS version 8.0.0 provided by the *XMM-Newton* SOC. The *Chandra* observations of APM 08279+5255 were analyzed using the standard software CIAO 4.1 provided by the CXC. A log of the observations that includes observation dates, observed count rates, total exposure times, and observational identification numbers is presented in Table 1.

We note that the count rate and total number of counts ($\sim$ 40,918 counts from all *XMM-Newton* observations) for APM 08279+5255 are the highest of any BAL quasar X-ray spectrum observed to date. This can be compared to the typical total number of 0.5–8 keV counts detected in BAL quasars obtained from the Sloan digital sky survey data release 5 that ranges between a few to $\sim$ 200 counts (Gibson et al. 2009).

For the reduction of the *XMM-Newton* observations we filtered the pn (Strüder et al. 2001) and MOS (Turner

---

[5] The WWW sites listing the updates are located at `http://xmm2.esac.esa.int/external/xmm_sw_cal/calib/`, respectively. `http://asc.harvard.edu/ciao/releasenotes/history.html` and

et al. 2001) data by selecting events corresponding to instrument `PATTERNS` in the 0–4 (single and double pixel events) and 0–12 (up to quadruple pixel events) ranges, respectively. Several moderate-amplitude background flares were present during the *XMM-Newton* observations of APM 08279+5255. The pn and MOS data were filtered to exclude times when the full-field-of-view count rates exceeded 20 cnts s^{-1} and 4 cnts s^{-1}, respectively. The extracted spectra from the pn and MOS were grouped to obtain a minimum of 100 counts in each energy bin, allowing use of χ^2 statistics. Background spectra for the pn and MOS detectors were extracted from source-free regions near APM 08279+5255.

The pn and MOS spectra were fit with a variety of models employing `XSPEC` version 12.5 (Arnaud 1996). The energy ranges used for fitting the pn and MOS data were 0.2–10 keV and 0.4–10 keV, respectively. We performed spectral fits to the pn spectra alone and to the pn and MOS data simultaneously. Both approaches resulted in values for the fitted parameters that were consistent within the errors, however, the fits to the higher quality pn data alone provided higher quality fits as indicated by the reduced χ^2 values of these fits. We therefore consider the results from the fits to the pn data alone more reliable especially for characterizing the properties of the X-ray absorption features.

For the reduction of the *Chandra* observations we used standard CXC threads to screen the data for status, grade, and time intervals of acceptable aspect solution and background levels. The pointings placed APM 08279+5255 on the back-illuminated S3 chip of ACIS. To improve the spatial resolution we removed a $\pm\,0\overset{''}{.}25$ randomization applied to the event positions in the CXC processing and employed a sub-pixel resolution technique developed by Tsunemi et al. (2001).

In both the *XMM-Newton* and *Chandra* analyses we tested the sensitivity of our results to the selected background and source-extraction regions by varying the locations of the background regions and varying the sizes of the source-extraction regions. We did not find any significant change in the background-subtracted spectra. For all models of APM 08279+5255 we included Galactic absorption due to neutral gas with a column density of $N_{\rm H}$=3.9 $\times\,10^{20}$ cm^{-2} (Stark et al. 1992). All quoted errors are at the 90% confidence level unless mentioned otherwise.

2.2. Chandra *and* XMM-Newton *Spectral Analysis of APM 08279+5255*

We first fitted the *Chandra* and *XMM-Newton* spectra of APM 08279+5255 with a simple model consisting of a power law with neutral intrinsic absorption at $z = 3.91$ (model 1 of Table 2). These fits are not acceptable in a statistical sense as indicated by the reduced χ^2. The residuals between the fitted simple absorbed power-law model and the data show significant absorption for energies in the observed-frame band of < 0.6 keV (referred to henceforth as low-energy absorption) and 2–5 keV (referred to henceforth as high-energy absorption).

To illustrate the presence of these low- and high-energy absorption features, we fit the spectra from observed-frame 4.5–10 keV with a power-law model (modified by Galac-

tic absorption) and extrapolated this model to the energy ranges not fit. The residuals of these fits are shown in Figures 1 and 2. Significant low- and high-energy absorption is evident in all observations.

We proceed by fitting the spectra of APM 08279+5255 with the following models: 1) absorbed power-law (APL), 2) absorbed power-law with a notch (APL+No), 3) ionized-absorbed power-law with a notch (IAPL+No), 4) absorbed power-law with an absorption edge (APL+Ed), 5) ionized-absorbed power-law with an absorption edge (IAPL+Ed), 6) absorbed power-law with two absorption lines (APL+2AL), 7) ionized-absorbed power-law with two absorption lines (IAPL+2AL), 8) absorbed power-law with two intrinsic ionized absorbers (APL + 2IA), and 9) absorbed power-law with with two partially covered intrinsic ionized absorbers (APL+PC*(2IA)). The XSPEC notations for these models are given in the notes of Tables 2 and 3.

The results from fitting these models to the three *XMM-Newton* and two *Chandra* spectra are presented in Tables 2 and 3. For spectral fits using models 3, 5, and 7 the low-energy absorption is modeled using the photo-ionization model `absori` contained in `XSPEC` (Done et al. 1992). We note that the `absori` model is just a first approximation to what is likely a more complex situation. As an independent check of the accuracy of the fits that used the `absori` model we also repeated several of these fits using the warm-absorber model `XSTAR` (Kallman et al. 1996; Kallman & Bautista 2001). `XSTAR` calculates the physical conditions and emission spectra of photoionized gases. In the current analysis we use a recent implementation of the `XSTAR` model that can be used within `XSPEC`.

In most epochs, models APL+2AL and IAPL+2AL that included two absorption lines provided significant improvements to the fits compared to models that included an absorption edge. Specifically, the F-test indicates the significance of the improvements of the IAPL+2AL model compared to the IAPL+ Ed model to be $\gtrsim 99.99\%$ ($\Delta\chi^2 = 42.5$), $\gtrsim 84\%$ ($\Delta\chi^2 = 6.4$), $\gtrsim 74\%$ ($\Delta\chi^2 = 6.3$), $\gtrsim 99\%$ ($\Delta\chi^2 = 15.6$), and $\gtrsim 99.7\%$ ($\Delta\chi^2 = 17.1$), for four additional parameters in epochs 1 through 5, respectively.

We note that the X-ray BALs in the 1.5–3.6 keV band (observed-frame) correspond to a significant detection following the criteria described in §3 of Vaughan & Uttley (2008). Specifically, we find the ratio of the total equivalent widths[6] of the absorption features to their uncertainty to be $EW/\sigma_{EW} \gtrsim 3$ in every observation (see models 6 and 7 in Table 2).

As indicated in the results of the spectral fits shown in Table 2, the energies and widths of the absorption lines of models APL+2AL and IAPL+2AL vary significantly between several epochs. This is also suggested by the residuals shown in Figures 1 and 2, where we indicate with arrows the locations of several of the best-fit energies of the absorption lines.

To estimate the significances of variations of the best-fit energies ($E_{\rm abs}$) and widths ($\sigma_{\rm abs}$) of the absorption lines between epochs we calculated the χ^2 confidence contours of these best-fit parameters.

We first focus on epochs 1 and 5 where the high-energy absorption lines appear to be narrower than in other

---

[6] The equivalent width (EW) is defined as $EW = \int \frac{F_c - F_E}{F_c} dE$, where F_c is the continuum flux and F_E is the flux in the absorber.

epochs (see Figures 1 and 2) and also show variability in energy and width. In Figure 3 we show the 68%, 90%, and 99% χ^2 confidence contours of E_{abs} versus normalization of the first and second absorption lines (APL + 2 AL model) in epoch 1 (top panel) and epoch 5 (bottom panel). Since the 99% and 95% confidence contours of the second absorption line (component $abs2$) between epochs 1 and 5, respectively, do not overlap in energy we conclude that a significant change occurred at the $> 99.9\%$ confidence level of the energy of the second absorption line between these epochs.

In Figure 4 we show the 68%, 90% and 99% χ^2 confidence contours of E_{abs} versus σ_{abs} of the first and second absorption lines (APL + 2 AL model) in epochs 1 and 5. The probability that the energy-width parameters of the first absorption line are the same between epochs 1 and 5 (null probability) is $\lesssim 1 \times 10^{-4}$ [7].

An additional significant variation of particular interest is found between epochs 3 and 4 that are separated by only 3.3 days in the rest frame. The 0.2–10 keV pn count rate of APM 08279+5255 varied between epochs 3 and 4 by 36.8 ± 0.3 %. We investigated whether the X-ray BALs varied in this 3.3 day period. In Figure 5 we show the 68%, 90% and 95% χ^2 confidence contours of E_{abs} versus σ_{abs} of the first absorption line (APL + 2 AL model) in epoch 3 (dotted line) and epoch 4 (solid line). The 95% confidence contours of epoch 3 almost touch the 90% confidence contours of epoch 4. The probability that the energy-width parameters of the first absorption line (model 7; Table 2) are the same between epochs 3 and 4 (null probability) is $\lesssim 0.05 \times 0.10 = 5 \times 10^{-3}$.

In Table 3 we present results from spectral fits that attempt to model the high-energy absorption with two outflowing ionized absorbers that are either completely covering the source (model 8) or are partially covering it (model 9). For spectral fits using models 8 and 9 the high-energy absorption in modeled using XSTAR. The low-energy absorption is modeled with a stationary neutral absorber. For epochs 1 and 5 we find that the combined covering factor of the highly ionized absorbers is close to unity. This is expected since the detected ionized absorption lines in epochs 1 and 5 are narrower than the ones detected in the other epochs whereas the presence of any significant direct component (emission that does not get absorbed by the outflowing material) would have diluted any narrow absorption lines. For epochs 2, 3 and 4 the spectral fits (model 9 of Table 3) do allow for an emitted component that is not absorbed by the ionized outflowing material.

Our fits with XSTAR indicate an outflowing X-ray absorbing medium with ionization parameters ranging between $\log\xi = 2.9$ [8] and $\log\xi = 3.9$ (model 8 of Table 3). The two strongest iron lines for this highly ionized absorbing medium have rest (or laboratory) energies of 6.70 keV (Fe XXV $1s^2 - 1s2p$) and 6.97 keV (Fe XXVI $1s - 2p$). In general the Fe XXV $1s^2 - 1s2p$ line will be stronger than the Fe XXVI $1s - 2p$ line for a medium with $2.75 \lesssim \log\xi \lesssim 4.0$

(see Figure 3 of Saez et al. 2009).

We emphasize that the photo-ionization models used in our analysis (i.e., absori and XSTAR) do not consider possible velocity gradients in the outflowing absorber and therefore cannot provide realistic models of the X-ray BALs. We attempt to mimic the velocity broadening of the lines by introducing in the XSTAR model large turbulent velocities of $v_{turb} = 10,000$ km s^{-1} for epochs 1 and 5 and $v_{turb} = 30,000$ km s^{-1} for epochs 3, 4 and 5.

3. DISCUSSION

3.1. Short- and Long-Term Variability of APM 08279+5255

As we showed in §2 the 0.2–10 keV pn count-rate of APM 08279+5255 varied by $\sim 36.8 \pm 0.3$ % between epochs 3 and 4. From a light-travel time argument we estimate that the observed short-term variability between epochs 3 and 4 implies a size-scale of the X-ray emission region of the order of $l_{var} = c\Delta t/(1 + z) \sim 7.4 \times 10^{15}$ cm. We compare this emission-region size scale to the radius of the innermost stable circular orbit (r_{ISCO}) which for Schwarzschild and Kerr (maximally spinning) black holes are $6r_g$ and r_g, respectively, where $r_g = GM/c^2$ is the gravitational radius. For APM 08279+5255 we assume $M_{BH} \sim 10^{12} M_\odot \mu_L^{-1}$, where $\mu_L \sim 100$ (Egami et al. 2000).[9] We find that $r_{ISCO} = 4.5 \times 10^{15}$ cm for the case of a Schwarzschild black hole which is comparable to the size-scale of the X-ray emitting region implied by our light-travel time argument. This result is consistent with recent X-ray and UV (rest-frame) monitoring observations of the $z = 2.32$ gravitationally lensed quasar HE 1104−1805 that have constrained the size of the X-ray emitting region in this object to be smaller than $6r_g$ and the size of the UV emission region to be $\sim 30r_g$ based on the analysis of the microlensed light-curves of the lensed images (Chartas et al. 2009). A hint to the cause of the spectral variability can be seen in Figure 6 where we show the three overplotted XMM-Newton spectra of APM 08279+5255.

The spectra between epochs 3 and 4 appear to differ over the entire observed energy band by approximately a constant. This type of behavior suggests that the cause of the variability is not the result of a change in the absorbing column density but is likely due to either a change in covering factor or a change in the ionizing flux from the central source.

As shown in Figure 6 the comparison between the epoch 2 and 3 XMM-Newton spectra, that are separated by ~ 5.4 years (observed-frame), indicates that they converge at energies above ~ 3 keV but diverge significantly below this value. This type of energy-dependent variation is indicative of a decrease in the absorbing column density between epochs 2 and 3 and is consistent with the results of our spectral analysis shown in Table 2. Since the relevant energy range (> 15 keV in the rest frame) is not significantly affected by neutral or ionized absorption, we interpret the variation between the epoch 2 and 3

---

[7] The product of the probabilities of being outside the confidence contours that barely touch (see Figure 4) is an upper limit to the null probability

[8] Throughout this paper we adopt the definition of the ionization parameter of Tarter et al. (1969) given by $\xi = \frac{L_{ion}}{n_H r^2} = \frac{4\pi}{n_H} \int_{1Rdy}^{1000Rdy} F_\nu d\nu$, where n_H is the hydrogen number density, and r is the source-cloud separation.

[9] See, however, Riechers et al. (2009), who find a magnification of $\mu_L \sim 4$. Riechers et al. (2009) also use the observed width of the CIV line to obtain a black-hole mass of $M_{BH} \sim 10^{11} \mu_L^{-1} M_\odot$.

XMM-Newton spectra as an indication that the intrinsic unabsorbed luminosity of APM 08279+5255 has not significantly varied between these two observations and that most of the observed changes in flux result from changes in the opacities of the low and/or high-ionization absorbers.

In Figure 7 we over-plot the epoch 1 and epoch 5 *Chandra* spectra that are separated by ∼ 5.9 years (observed-frame). The spectra appear to converge at energies below ∼ 0.7 keV and above ∼ 5 keV and significantly differ between these energies. As shown in our spectral analysis, the X-ray BALs varied significantly between these two epochs which is consistent with the observed difference of the spectra between 0.7–3.6 keV seen in Figure 7. The variability of the absorption between epochs 1 and 5 can in general be caused by at least three factors: (a) transverse motion of the absorber across the continuum source, (b) changes in the opacity of the absorber, and (c) changes in the velocity structure of the absorber. Epochs 1 and 5 are separated by 2150 days which is significantly longer than the expected timescale of variability due to transverse motion and also longer than the expected flow timescale. We therefore cannot reach a firm conclusion regarding the cause of the variability between epochs 1 and 5. The significant differences in timescales, however, imply that it is unlikely that the variability is being produced by the same absorber moving across our line of sight.

To better illustrate the flux variability of APM 08279+5255 we show the ratios of the observed and best-fit modeled (using model 6 of Table 2) flux densities F_i/F_j between the three *XMM-Newton* observations in Figure 8 and between the two *Chandra* observations in Figure 9, where i and j represent the epochs compared, F is the flux density in units of counts s^{-1} keV^{-1} and Δt is the observed-frame time between epochs. We first focus on the short-term variability between epochs 3 and 4 shown in Figure 8. We notice that the variability of the flux density is to first order independent of energy over the observed 0.5–10 keV band with the exception of apparent variability in the region of 1.5–3.6 keV (observed-frame) near the Fe BALs. A plausible explanation of the energy independence of the short-term variability of the flux density may involve motion of the highly ionized absorbing outflow perpendicular to our line of sight. This motion may change the covering factor resulting in possible energy-independent variability of the flux density. A second possible explanation is a change in the ionizing flux of the central source. Our spectra fits that assumed a model that includes emission through two ionized absorbers and emission that is not absorbed by the ionized absorber (model 9 of Table 3) suggest a possible decrease in the total covering factor of the ionized absorbers between epochs 3 and 4. Unfortunately the limited S/N of the current spectra provide poor constraints on the covering factors and therefore the implied change in covering factor between epochs 3 and 4 can only be considered suggestive.

We second center on the long-term variability between epochs 2 and 3 shown in Figure 8. The variability of the flux density between these epochs becomes large below ∼ 2 keV, however, no significant variability is detected above this energy. A possible explanation of such energy dependent variability is a decrease in column density between epochs 2 and 3.

We finally comment on the long-term variability between epochs 1 and 5 shown in Figure 9. We note that the flux density appears to have varied by a larger factor near the region of the Fe BALs that extends above ∼ 1.5 keV (observed frame). A possible explanation for this flux-density variability between these epochs is a change in the properties of the outflowing ionized absorbers. This interpretation is consistent with the results of our previous spectral analysis that showed a significant change in the energies and widths of the absorptions lines (see Figures 3 and 4).

3.2. *Mass-Outflow Rate and Efficiency of the Outflow*

Our *XMM-Newton* and *Chandra* observations of APM 08279+5255 provide constraints on the velocity, column density, and location of the X-ray BAL material that allow us to estimate the mass-outflow rate from the expression:

$$\dot{M}_i = 4\pi r_i (r_i/\Delta r_i) N_{\mathrm{H},i} m_p v_{wind,i} f_{c,i}. \quad (1)$$

where Δr_i is the thickness of the absorber at radius r_i, $N_{\mathrm{H},i}$ is the hydrogen column density, $v_{\mathrm{wind},i}$ is the outflow velocity of the X-ray absorber, $f_{c,i}$ is the global covering factor of the absorber, and i indicates the absorbing component. Combining the constraints on the mass-outflow rate and the bolometric luminosity we can estimate the efficiency of the quasar outflow. The efficiency is defined as the ratio of the rate of kinetic energy injected into the interstellar medium (ISM) and intergalactic medium (IGM) by the outflow to the quasar's bolometric luminosity, i.e.,

$$\epsilon_{\mathrm{k},i} = \frac{1}{2}\frac{\dot{M}_i v_{\mathrm{wind},i}^2}{L_{\mathrm{Bol}}} = 2\pi f_{c,i} r_i (r_i/\Delta r_i) N_{\mathrm{H},i} m_p \frac{v_{\mathrm{wind},i}^3}{L_{\mathrm{Bol}}} \quad (2)$$

where L_{Bol} is the bolometric luminosity of the quasar.

The best-fit values of the equivalent widths of the X-ray absorption lines (assuming model 6 of Table 2) were used to estimate the hydrogen column densities N_{H} of the X-ray BALs using a curve-of-growth analysis (e.g., Spitzer 1978). For our crude calculation we assumed b parameters of the order of the observed widths of the lines where, $b = \sqrt{2}\sigma_u$ and σ_u is the velocity width of the line. The bulk outflow velocities of each outflow component were inferred from the best-fit values of the energies of the blueshifted absorption lines obtained by spectral fits to the data assuming model 6 of Table 2. To convert from line energies to outflow velocities we used the relativistic Doppler formula assuming that the high-energy absorption lines are the result of resonance absorption from ions of Fe XXV in a gas with solar abundances, and the angle between our line of sight and the outflow direction is zero. For estimating the outflow efficiency of APM 08279+5255 we assumed $L_{\mathrm{bol}} = 7 \times 10^{15}\mu_L^{-1}L_\odot$ (Irwin et al. 1998; Reichers et al. 2009). We assume a conservatively wide range for the covering factor of f_c=0.1–0.3 based on the observed fraction of BAL quasars (e.g., Hewett & Foltz 2003). We obtained a constraint on the covering fraction of the flow by placing limits on the presence of any emission components of the lines. Crudely the ratio of the emission to absorption equivalent widths is proportional to the global covering factor f_c. The tightest upper bound is found for the

XMM-Newton observation of APM 08279+5255 in epoch 3. We find that $EW_{em1}/EW_{abs1} < 0.24$ at the 90% confidence level assuming model 6 of Table 2 and we expect $f_c \propto EW_{em1}/EW_{abs1}$. We note that the covering factor f_c will depend on the fluorescence yields of the ionized absorber which for Fe XXV and Fe XXVI are 0.5 and 0.7, respectively (e.g., Krolik & Kallman 1987). For this crude estimate we included a narrow emission line in model 6 at a rest-frame energy of 6.7 keV. The exact relevant energy of the emission line to consider is probably geometry dependent. For estimating the outflow efficiency we assumed a fraction $r/\Delta r$ ranging from 1–10 based on theoretical models of quasar outflows (e.g., Proga & Kallman 2000). Assuming that the maximum outflow velocity is produced by gas that has reached its terminal velocity one obtains the approximation $R_{launch} \sim R_s(c/v_{wind})^2$, where v_{wind} is the observed outflow velocity. Based on our estimated maximum outflow velocity ($v = 0.76~c$) we expect r to be similar to R_{launch} and range between 3 R_s and 15 R_s (see Figure 4 of Saez et al. 2009). We note that the short term variability time-scale of the X-ray BALs (3.3 d in rest-frame) is consistent with a launching radius of a few times R_S.

We used a Monte Carlo approach to estimate the errors of $\dot{M}_i$ and ϵ_k. The values of f_c, $r/\Delta r$, and r_i were assumed to have uniform distributions within their error limits. The values of N_H were assumed to have normal distributions within their error limits. By multiplying these distributions and with the appropriate constants from equations 1 and 2 we obtained the distributions of $\dot{M}_i$ and ϵ_k. We finally determined the means of the distributions of $\dot{M}_i$ and ϵ_k and estimated the 68% confidence ranges.

In Table 4 we present the outflow velocities, the column densities, the mass-outflow rates and the efficiencies of the outflowing components.

3.3. *Driving Mechanism of X-ray BALs*

One of the major unanswered questions in current theoretical and numerical models of quasar winds involves explaining how highly ionized outflows of X-ray absorbing material become accelerated to near-relativistic velocities. The main problem is that for radiatively driven winds the magnitude of the force on an absorber is a function of its ionization state. As the ionization parameter of the absorber increases, fewer resonant transitions are available to absorb photons from the source, thus resulting in a weaker driving force. Chelouche & Netzer (2001) have explored the dependence of the radiation driving force on the ionization parameter of the outflowing gas and they conclude that for a highly ionized X-ray absorbing gas, the average force multipliers are close to 10.

Most current theoretical work on radiative acceleration in quasars has focused on interpreting the outflows of UV absorbers (e.g, Murray et al. 1995; Proga et al. 2000; Proga et al. 2004; Everett 2005), however; there are no self-consistent models that can explain the acceleration mechanism that leads to the near-relativistic outflows of X-ray absorbing material.

A clue to understanding the acceleration process of the wind in APM 08279+5255 is perhaps provided by the observed large difference between the maximum velocities of the UV ($v_{UV} \sim 0.04c$; e.g., Srianand & Petitjean 2000) and X-ray ($v_{X-ray} \sim 0.43$–$0.76c$) absorbers. One possible explanation of the difference between the UV and X-ray outflow velocities is that the UV and X-ray BALs are produced by different absorbers, with UV emission from the accretion disk driving the UV absorbers and X-ray emission from the hot corona contributing to the acceleration of the X-ray absorbers. If the X-ray absorbers are partly driven by radiation from the hot corona we might expect to detect a correlation between the properties of the X-ray BALs and the properties of the X-ray spectrum. For example, we might expect the maximum outflow velocity of the X-ray absorbers to depend on the shape of the X-ray spectrum that at first order can be represented with the X-ray photon index (Γ).

The minimum and maximum projected velocities (v_{min}, v_{max}) of the outflow are estimated from the minimum and maximum energy ranges (E_{min}, E_{max}) of the high-energy absorption features in APM 08279+5255 assuming that the high-energy X-ray BALs are produced by the resonance transition Fe XXV ($1s^2 - 1s2p$). We obtained E_{min} and E_{max} from our spectral fits assuming the two absorption-line (APL+2AL) model. Specifically, based on the best-fit values of the APL+2AL model (model 6; Table 2), we obtain $E_{min} = E_{abs1} - 2\sigma_{abs1}$ and $E_{max} = E_{abs2} + 2\sigma_{abs2}$. The values of E_{min} and E_{max} are presented in Table 5.

In Figure 10 we show the maximum outflow velocity observed from APM 08279+5255 as a function of X-ray photon index based on the *XMM-Newton*, *Chandra*, and *Suzaku* observations. We notice a possible trend between the photon index and the maximum outflow velocity in the sense that flatter X-ray spectra appear to result in lower outflow velocities. One possible explanation is that flatter X-ray spectra over-ionize the X-ray absorber resulting in a decrease of the force multiplier and a lower outflow velocity. If this trend is confirmed with future observations it would imply that the dominant acceleration mechanism responsible for the near-relativistic velocities of the X-ray outflowing gas in BAL quasars is indeed radiation driving as opposed to magnetic driving.

We investigated our hypothesis of the origin of the possible $\Gamma - v_{max}$ correlation by calculating the force multiplier as a function of the incident spectral energy distribution (SED). The force multiplier represents the ratio by which the bound-bound (line) and bound-free (continuum) opacity increases the radiation force relative to that produced by Thomson scattering alone.

We performed calculations of force multipliers assuming a thin slab illuminated by an ionizing continuum using the CLOUDY code. We compared our results to those of Arav et al. (1994) and Everett et al. (2005) who have used a similar approach to ours. In general our computations are in good agreement. We performed calculations assuming the SED is a power-law extending from the UV (or 1 Ryd $\sim$13.6 eV) to hard X-rays (or 10^4 Ryd $\sim$100 keV). For our calculations we assume SEDs with two different values of the power-law photon index. A "soft" ($\Gamma = 2.1$) and a "hard" ($\Gamma = 1.7$) SED. For each SED we calculated the continuum (M_C) and the line (M_L) components of the force multiplier. M_L depends on an additional parame-

---

[10] The dimensionless optical depth is $t = n_e\sigma_T v_{th}/(dv/dr)$, where, n_e is the electron number density, σ_T is the Thomson cross section and v_{th}

ter, t, [10] which is commonly referred to as the "effective electron optical depth" and encodes the dynamical information of the wind in the radiative acceleration calculation (see equation 2.5 of Arav & Li 1994). For our calculations we have assumed $\log t = -7$. In Figure 11 we show the M_C and M_L components of the force multiplier as a function of the ionization parameter and for the soft and hard SED cases. Our simple ionized absorber model indicates that an increase of the photon-index from 1.7 to 2.1 of the incident spectrum will result in a large increase of the force multiplier. This result is consistent with the possible trend between Γ and v_{max} shown in Figure 10.

Theoretical models of AGN outflows (e.g., Murray et al. 1995; Chelouche & Netzer 2003) and our observations of APM 08279+5255 suggest that the UV BAL gas could be shielded from the driving radiation by an absorbing medium surrounding the central source. We included the effect of such a shield on our calculated values of the force multiplier by assuming that the soft and hard SEDs are attenuated by an absorber with $\log N_H = 22.8$ and the temperature at the illuminated face of the absorbing shield has the value $\log T[K] = 5.0$ ($\log \xi \sim 1.4$). As shown in Figure 11, M_C decreases in the absorbed-SED case for $\log \xi \lesssim 2$, whereas, M_L increases in the absorbed-SED case. We find that M_L increases by almost an order of magnitude in the absorbed-SED case when the photon index increases from 1.7 to 2.1. In Figure 11 we show that in addition to the SED and t parameter, the force multiplier depends strongly on the ionization parameter. In Figure 11b the force multiplier for a shielded outflow drops from about 1000 to 500 between $\log \xi$ of 2–2.8 and drops from about 500 to 1 between $\log \xi$ of 2.8–3, i.e., similar to the observed range of the ionization parameter of APM 08279+5255. We expect that we observe the ionized X-ray absorber of APM 08279+5255 while it has obtained its terminal velocity. The observed large value of the ionization parameter of APM 08279+5255 may therefore not be representative of the ionization parameter during the initial acceleration phase of the absorber.

We note that our assumption that the driving force on the high-energy absorbers is produced primarily by X-rays is plausible since the short term variability time-scale of the X-ray BALs of APM 08279+5255 suggest a launching radius of $\lesssim 10 R_S$ (e.g, Chartas et al. 2002; Saez et al. 2009; this work) and recent studies of AGN employing the microlensing technique indicate that the X-ray emission region of the hot corona in AGNs is compact with a half-light radius of a few R_S and their UV regions are roughly a factor of ten larger (e.g, Morgan et al 2008; Chartas et al. 2009). Therefore UV radiation is not expected to contribute initially at small radii to driving the X-ray absorbing outflow.

If the $\Gamma - v_{max}$ trend is confirmed with additional observations we plan to produce a more sophisticated model that will include more realistic kinematic, ionization and absorption properties of the outflow.

3.4. Constraints on Outflow Direction

The observed maximum projected outflow velocities of the X-ray BALs combined with the constraint that the maximum velocity of the X-ray absorber along the outflow

direction must satisfy $v_{outflow} < c$ leads to a constraint on the maximum angle between the outflow direction and the observed line of sight through the absorber(θ_{max}). The best-fitted values of the ionization parameter for the outflowing absorbers (see model 8 of Table 3) lie in the range of $2.9 \lesssim \log \xi \lesssim 3.9$ and imply that the high-energy absorption is the result of resonance absorption from ions of Fe XXV and/or Fe XXVI. Since the present X-ray spectra cannot distinguish between these ionization stages we estimate the angle between the outflow direction and our line of sight considering that the X-ray BALs are produced by resonance transitions of either Fe XXV ($1s^2-1s2p$), Fe XXV ($1s^2 - 1s3p$), Fe XXVI ($1s - 2p$) and Fe XXVI ($1s - 3p$). In Figure 12 we show the outflow velocity versus the angle between the direction of the outflowing absorber and our line of sight through the absorber. The outflow velocities were calculated using the relativistic Doppler formula for the case of the maximum rest-frame energy of the X-ray BALs of $E_{max} = 17.9$ keV (see Table 5) observed in epoch 3. For the case where the X-ray BALs are produced by the resonance transition of Fe XXV ($1s^2 - 1s2p$) the detected projected maximum outflow velocity of $v_{max} \sim 0.76c$ leads to the constraint of $\theta_{max} \lesssim 22°$. Such a small angle is consistent with the unification scheme of BAL and non-BAL quasars that posits that BAL quasars are viewed almost along the outflow direction.

4. CONCLUSIONS

We have presented results from an analysis of three *XMM-Newton* and two *Chandra* observations of the $z = 3.91$ BAL quasar APM 08279+5255. The main goals of these observations were to study the kinematic and photoionization properties of the wind in order to assess whether it plays an important role in controlling the evolution of the host galaxy and central black hole. Additional objectives included understanding the mechanism that drives the X-ray absorbers to near-relativistic velocities and constraining the geometry of the outflow.

The main conclusions of our spectral and timing analyses are the following:

(a) X-ray BALs lying in the range of 1.5–3.6 keV (observed frame) are detected at the greater than 99.9% confidence level in all five observations of APM 08279+5255. We note that a recent analysis of three *Suzaku* observations of APM 08279+5255 also shows significant detections of X-ray BALs in all three observations (Saez et al. 2009).

(b) Based on our spectral analysis we identify the following components of the outflow. First, a highly ionized X-ray absorbing material with an ionization parameter in the range of $2.9 \lesssim \log \xi \lesssim 3.9$ and a column density of $\log N_H \sim 23$ outflowing at velocities of up to 0.76 c, and second a low-ionization X-ray absorbing gas with a column density of $\log N_H \sim 22.8$ that may constitutes the X-ray shielding gas that is thought to protect the UV absorber from becoming over-ionized. Models that include partial covering result in even larger column densities of the ionized absorber of up to $\log N_H \sim 24$, however, we caution that these values are not well constrained (see model 9 of Table 3) by the spectral fits. We note that no iron overabundance is required to fit the X-ray spectra of APM 08279+5255 consistent with the spectral analysis

is the thermal velocity of the gas. The line force multiplier increases with decreasing t.

of previous observations of this object.

(c) Significant variability of the X-ray continuum and X-ray BALs over short and long time-scales is detected. Specifically, we detect a $\sim 36.8 \pm 0.3$ % change of the 0.2–10 keV pn count-rate between epochs 3 and 4 that are separated by only 3.3 days (proper-time). Based on a simple light-travel time argument this variability time-scale implies a radius of the emission region of $\sim 7.4 \times 10^{15}$ cm which is comparable to $r_{\mathrm{ISCO}} = 4.5 \times 10^{15}$ cm for the case of a Schwarzschild black hole in APM 08279+5255. We speculate based on the energy independent spectral change between epochs 3 and 4 (with the exception of the Fe BAL region) that the cause of this variability is a change in the covering fraction as the outflowing absorbing material moves across our line of sight. Significant changes in the flux densities between epochs 2 and 3 that are separated by ~ 5.4 years (observed-frame) are detected. The variation of flux density is significant below 3 keV (observed frame) showing a increase toward lower energies but is near zero above 3 keV. This type of energy-dependent change suggests that the intrinsic unabsorbed luminosity of APM 08279+5255 has not significantly varied between these epochs and the long-term variability is the result of a decrease in the opacity of the absorber. This interpretation is consistent with the results of our spectral analysis.

(d) Assuming our interpretation that the high-energy X-ray BALs are produced by resonance transitions of highly-ionized iron we estimate the mass-outflow rate and efficiency of the outflow to have varied over a period of 1.2 years (proper-time) between 16^{+12}_{-8} $M_\odot$ yr^{-1} and 64^{+66}_{-40} $M_\odot$ yr^{-1} and $0.18^{+0.15}_{-0.11}$ to $1.7^{+1.9}_{-1.2}$, respectively.

(e) The detected projected maximum outflow velocity of $v_{\mathrm{max}} \sim 0.76c$ leads to a constraint on the angle between the outflow direction and the observed line of sight through the absorber of $\theta_{\mathrm{max}} \lesssim 22°$ (assuming Fe XXV$(1s^2-1s2p)$) and $\theta_{\mathrm{max}} \lesssim 26°$ (assuming Fe XXVI$(1s-2p)$). Such a small angle is consistent with the unification scheme of BAL and non-BAL quasars that posits that BAL quasars are viewed almost along the outflow direction.

(f) A possible trend is found between the X-ray photon index and the maximum outflow velocity of the ionized X-ray absorber in the sense that flatter X-ray spectra appear to result in lower outflow velocities. One possible explanation is that flatter X-ray spectra over-ionize the X-ray absorber resulting in a decrease of the force multiplier of the X-ray absorber and thus a lower outflow velocity.

REFERENCES

Arav, N., & Li, Z.-Y. 1994, ApJ, 427, 700

Arav, N., Li, Z.-Y., & Begelman, M. C. 1994, ApJ, 432, 62

Arnaud, K. A. 1996, ASP Conf. Ser. 101: Astronomical Data Analysis Software and Systems V, 5, 17

Blandford, R. D., & Payne, D. G. 1982, MNRAS, 199, 883

Blandford, R. D., & Znajek, R. L. 1977, MNRAS, 179, 433

Braito, V., et al. 2007, ApJ, 670, 978

Chartas, G. 2000, ApJ, 531, 81

Chartas, G., Brandt, W. N., Gallagher, S. C., & Garmire, G. P. 2002, ApJ, 579, 169

Chartas, G., Brandt, W. N., & Gallagher, S. C. 2003, ApJ, 595, 85

Chartas, G., Brandt, W. N., Gallagher, S. C., & Proga, D. 2007a, AJ, 133, 1849

Chartas, G., Eracleous, M., Dai, X., Agol, E., & Gallagher, S. 2007b, ApJ, 661, 678

Chartas, G., Kochanek, C. S., Dai, X., Poindexter, S., & Garmire, G. 2009, ApJ, 693, 174

Chelouche, D., & Netzer, H. 2001, MNRAS, 326, 916

Chelouche, D., & Netzer, H. 2003, MNRAS, 344, 233

Ciotti, L., & Ostriker, J. P. 2007, ApJ, 665, 1038

Di Matteo, T., Springel, V., & Hernquist, L. 2005, Nature, 433, 604

Done, C., Mulchaey, J. S., Mushotzky, R. F., & Arnaud, K. A. 1992, ApJ, 395, 275

Elvis, M. 2000, ApJ, 545, 63

Egami, E., Neugebauer, G., Soifer, B.T., Matthews, K., Ressler, M., Becklin, E. E., Murphy, T.W., Jr., & Dale, D.A. 2000, ApJ, 535, 561

Everett, J. E., & Ballantyne, D. R. 2004, ApJ, 615, L13

Everett, J. E. 2005, ApJ, 631, 689

Fabian et al. 2009, MNRAS, 396, 1449S

Gallagher, S. C., Brandt, W. N., Chartas, G., & Garmire, G. P. 2002, ApJ, 567, 37

Ganguly, R., & Brotherton, M. S. 2008, ApJ, 672, 102

Garmire, G. P., Bautz, M. W., Ford, P. G., Nousek, J. A., & Ricker, G. R. 2003, Proc. SPIE, 4851, 28

Gibson, R. R., et al. 2009, ApJ, 692, 758

Granato, G. L., De Zotti, G., Silva, L., Bressan, A., & Danese, L. 2004, ApJ, 600, 580

Hopkins, P. F., Hernquist, L., Cox, T. J., Di Matteo, T., Martini, P., Robertson, B., & Springel, V. 2005, ApJ, 630, 705

Hopkins, P. F., Hernquist, L., Cox, T. J., Di Matteo, T., Robertson, B., & Springel, V. 2006, ApJS, 163, 1

Irwin, M. J., Ibata, R. A., Lewis, G. F., & Totten, E. J. 1998, ApJ, 505, 529

Jansen, F., Lumb, D., Altieri, B., et al. 2001, A&A, 365, L1

Jiang, L., Fan, X., Ivezić, Ž., Richards, G.T., Schneider, D.P., Strauss, M.A., & Kelly, B.C. 2007, ApJ, 656, 680

Krolik, J. H., & Kallman, T. R. 1987, ApJ, 320, L5

Kallman, T. R., Liedahl, D., Osterheld, A., Goldstein, & W., Kahn, S. 1996, ApJ, 465, 994

Kallman, T., & Bautista, M. 2001, ApJS, 133, 221

La Franca, F., Gregorini, L., Cristiani, S., de Ruiter, H., & Owen, F. 1994, AJ, 108, 1548

Laor, A., & Brandt, W. N. 2002, ApJ, 569, 641

Morgan, C. W.; Kochanek, C. S.; Dai, X.; Morgan, N. D.; Falco, E. E. 2008, ApJ, 689, 755.

Murray, N., Chiang, J., Grossman, S. A., & Voit, G. M. 1995, ApJ, 451, 498

Peacock, J.A., Miller, L., & Longair, M. S. 1986, MNRAS, 218, 265

Pounds, K. A., & Page, K. L. 2006, MNRAS, 372, 1275

Pounds, K. A., Reeves, J. N., King, A. R., Page, K. L., O'Brien, P. T., & Turner, M. J. L. 2003, MNRAS, 345, 705

Proga, D., & Kallman, T.R. 2004, ApJ, 616, 688

Proga, D., Stone J.M., & Drew J.E. 1998, MNRAS, 295, 595

Proga, D., Stone, J.M., & Kallman, T.R. 2000, ApJ, 543, 686

Riechers, D. A., Walter, F., Carilli, C. L., & Lewis, G. F. 2009, ApJ, 690, 463

Scannapieco, E., & Oh, S. P. 2004, ApJ, 608, 62

Schneider, D.P., van Gorkom, J.H., Schmidt, M., & Gunn, J. E. 1992, AJ, 103, 1451

Silk, J., & Rees, M. J. 1998, A&A, 331, L1

Spitzer, L. 1978, New York Wiley-Interscience, 1978. 333 p.

Springel, V., Di Matteo, T., & Hernquist, L. 2005, ApJ, 620, L79

Srianand, R. & Petitjean, P. 2000, A&A, 357, 414

Stark, A. A., Gammie, C. F., Wilson, R. W., Bally, J., Linke, R. A., Heiles, C., & Hurwitz, M. 1992, ApJS, 79, 77

Strüder, L., Briel, U., Dennerl, K., et al., 2001, A&A, 365, L18

Tarter, C. B., Tucker, W. H., & Salpeter, E. E. 1969, ApJ, 156, 943

Turner, M. J. L., Abbey, A., Arnaud, M., 2001, A&A, 365, L27

Tsunemi, H., Mori, K., Miyata, E., Baluta, C., Burrows, D. N., Garmire, G. P., & Chartas, G. 2001, ApJ, 554, 496

Vaughan S., & Uttley P. 2008, MNRAS, 390, 421.

TABLE 1

LOG OF OBSERVATIONS OF APM 08279+5255

Observation Date	Observatory	Observation ID	Time[a] (ks)	$N_{\rm sc}$[b] net counts	$f_{0.2-2}$[c] erg s^{-1} cm^{-2}	f_{2-10}[c] erg s^{-1} cm^{-2}
2002 February 24 (Epoch 1)	*Chandra*	2979	88.82	$5{,}627 \pm 75$	$1.8^{+0.1}_{-0.1}$	$4.3^{+0.1}_{-0.1}$
2002 April 28 (Epoch 2)	*XMM-Newton*	0092800201	83.46	$12{,}820 \pm 139$	$1.9^{+0.1}_{-0.1}$	$4.1^{+0.1}_{-0.1}$
2007 October 06 (Epoch 3)	*XMM-Newton*	0502220201	56.38	$11{,}400 \pm 114$	$2.5^{+0.1}_{-0.1}$	$3.9^{+0.1}_{-0.1}$
2007 October 22 (Epoch 4)	*XMM-Newton*	0502220301	60.37	$16{,}698 \pm 133$	$3.5^{+0.1}_{-0.1}$	$5.0^{+0.1}_{-0.1}$
2008 January 14 (Epoch 5)	*Chandra*	7684	88.06	$6{,}938 \pm 83$	$1.9^{+0.2}_{-0.2}$	$4.5^{+0.2}_{-0.2}$

[a]Time is the effective exposure time remaining after the application of good time-interval (GTI) tables and the removal of portions of the observation that were severely contaminated by background flaring.

[b]Background-subtracted source counts including events with energies within the 0.2–10 keV band. The source counts and effective exposure times for the *XMM-Newton* observations refer to those obtained with the EPIC PN instrument. See §2 for details on source and background extraction regions used for measuring $N_{\rm sc}$.

[c]The absorbed fluxes (in units of 10^{-13} ergs cm^{-2} s^{-1}) in the 0.2–2 keV and 2–10 keV observed-frame band are obtained using the model APL+2AL (model 6; §3). The errors are at the 68% confidence level.

TABLE 2
RESULTS FROM SPECTRAL FITS TO THE *Chandra* AND *XMM-Newton* OBSERVATIONS OF APM 08279+5255.

Model[a]	Parameter[c]	Values Epoch 1[d]	Values Epoch 2[d]	Values Epoch 3[d]	Values Epoch 4[d]	Values Epoch 5[d]
1.......	Γ	$1.74^{+0.06}_{-0.06}$	$1.94^{+0.05}_{-0.05}$	$2.11^{+0.05}_{-0.05}$	$2.14^{+0.04}_{-0.03}$	$1.94^{+0.07}_{-0.05}$
	N_{H}	$4.23^{+0.78}_{-0.73}$	$5.9^{+0.52}_{-0.49}$	$5.26^{+0.40}_{-0.38}$	$5.50^{+0.31}_{-0.30}$	$10.5^{+1.27}_{-1.58}$
	χ^2/ν	189.8/109	192.8/120	191.1/110	244.8/148	100.9/75
	$P(\chi^2/\nu)$[e]	2.6×10^{-6}	0.025	2.8×10^{-5}	2.6×10^{-6}	9.7×10^{-7}
2.......	Γ	$1.75^{+0.02}_{-0.02}$	$1.87^{+0.04}_{-0.05}$	$2.04^{+0.04}_{-0.04}$	$2.08^{+0.04}_{-0.03}$	$1.95^{+0.04}_{-0.04}$
	N_{H}	$4.6^{+0.84}_{-0.77}$	$6.19^{+0.51}_{-0.45}$	$5.39^{+0.39}_{-0.38}$	$5.64^{+0.29}_{-0.31}$	$10.85^{+1.30}_{-0.96}$
	$E_{\mathrm{notch}}[\mathrm{keV}]$	$8.04^{+0.10}_{-0.07}$	$11.24^{+0.50}_{-0.72}$	$11.62^{+0.44}_{-0.39}$	$12.91^{+1.30}_{-0.91}$	$8.49^{+0.2}_{-0.2}$
	$W_{\mathrm{notch}}[\mathrm{keV}]$	$0.23^{+0.06}_{-0.06}$	$7.70^{+0.90}_{-1.50}$	$8.87^{+1.28}_{-0.79}$	$11.85^{+2.29}_{-1.90}$	$0.16^{+0.07}_{-0.06}$
	$f_{\mathrm{notch}}[\mathrm{keV}]$	1	$0.21^{+0.04}_{-0.04}$	$0.21^{+0.04}_{-0.04}$	$0.16^{+0.03}_{-0.03}$	1
	χ^2/ν	151/107	122.9/117	117.4/107	175.8/145	83.2/73
	$P(\chi^2/\nu)$	3.2×10^{-3}	0.34	0.23	0.04	0.19
3.......	Γ	$1.78^{+0.06}_{-0.03}$	$1.92^{+0.05}_{-0.05}$	$2.08^{+0.05}_{-0.03}$	$2.10^{+0.04}_{-0.04}$	$1.94^{+0.05}_{-0.05}$
	N_{H}	$15.6^{+8.3}_{-8.6}$	$13.5^{+4.85}_{-4.49}$	$9.92^{+4.1}_{-4.1}$	$8.36^{+2.18}_{-3.45}$	$11.61^{+1.13}_{-1.58}$
	ξ	<0.18	150^{+120}_{-127}	86^{+192}_{-86}	32^{+97}_{-12}	<9
	$E_{\mathrm{notch}}[\mathrm{keV}]$	$8.0^{+0.1}_{-0.1}$	$11.15^{+0.69}_{-0.77}$	$11.54^{+0.60}_{-0.36}$	$12.82^{+0.77}_{-0.53}$	$8.54^{+0.2}_{-0.2}$
	$W_{\mathrm{notch}}[\mathrm{keV}]$	$0.25^{+0.06}_{-0.06}$	$8.12^{+1.42}_{-1.59}$	$8.94^{+1.17}_{-0.73}$	$11.78^{+2.29}_{-1.75}$	$0.14^{+0.07}_{-0.07}$
	$f_{\mathrm{notch}}[\mathrm{keV}]$	1	$0.18^{+0.04}_{-0.04}$	$0.20^{+0.04}_{-0.04}$	$0.16^{+0.03}_{-0.03}$	1
	χ^2/ν	146/106	112.7/116	114.1/106	175.4/144	79.5/72
	$P(\chi^2/\nu)$	6.1×10^{-3}	0.57	0.28	0.04	0.25
4.......	Γ	$1.72^{+0.06}_{-0.06}$	$1.88^{+0.05}_{-0.05}$	$2.07^{+0.04}_{-0.04}$	$2.12^{+0.03}_{-0.03}$	$1.95^{+0.06}_{-0.06}$
	N_{H}	$4.78^{+0.86}_{-0.70}$	$6.22^{+0.53}_{-0.46}$	$5.43^{+0.40}_{-0.39}$	$5.74^{+0.32}_{-0.31}$	$11.26^{+1.17}_{-1.11}$
	$E_{\mathrm{zedge}}[\mathrm{keV}]$	$7.66^{+0.17}_{-0.18}$	$7.57^{+0.16}_{-0.16}$	$7.33^{+0.18}_{-0.17}$	$7.10^{+0.15}_{-0.13}$	$7.60^{+0.25}_{-0.28}$
	τ_{zedge}	$0.40^{+0.11}_{-0.11}$	$0.43^{+0.09}_{-0.09}$	$0.38^{+0.09}_{-0.09}$	$0.30^{+0.07}_{-0.07}$	$0.21^{+0.09}_{-0.09}$
	χ^2/ν	144.7/107	121.9/118	133.9/108	186.4/146	83.4/73
	$P(\chi^2/\nu)$	8.9×10^{-3}	0.38	0.05	0.01	0.19
5.......	Γ	$1.72^{+0.06}_{-0.05}$	$1.94^{+0.05}_{-0.05}$	$2.13^{+0.04}_{-0.05}$	$2.16^{+0.04}_{-0.04}$	$1.95^{+0.08}_{-0.07}$
	N_{H}	$4.6^{+4.1}_{-0.7}$	$15.69^{+5.7}_{-5.4}$	$12.3^{+3.94}_{-4.11}$	$10.37^{+4.02}_{-2.66}$	$13.5^{+5.33}_{-3.66}$
	ξ	<77	242^{+315}_{-182}	194^{+252}_{-159}	93^{+209}_{-76}	<28
	$E_{\mathrm{zedge}}[\mathrm{keV}]$	$7.68^{+0.16}_{-0.11}$	$7.30^{+0.29}_{-0.23}$	$7.17^{+0.16}_{-0.09}$	$7.02^{+0.11}_{-0.12}$	$7.08^{+0.89}_{-0.78}$
	τ_{zedge}	$0.38^{+0.11}_{-0.10}$	$0.35^{+0.07}_{-0.08}$	$0.36^{+0.09}_{-0.08}$	$0.31^{+0.07}_{-0.07}$	$0.14^{+0.07}_{-0.09}$
	χ^2/ν	144.5/106	112.8/117	126.4/107	178.9/145	83.0/72
	$P(\chi^2/\nu)$	7.8×10^{-3}	0.59	0.10	0.03	0.18
6.......	Γ	$1.74^{+0.06}_{-0.05}$	$1.89^{+0.05}_{-0.05}$	$2.03^{+0.05}_{-0.06}$	$2.11^{+0.04}_{-0.03}$	$1.94^{+0.06}_{-0.06}$
	N_{H}	$4.89^{+0.80}_{-0.73}$	$6.29^{+0.55}_{-0.52}$	$5.41^{+0.41}_{-0.39}$	$5.74^{+0.32}_{-0.31}$	$11.35^{+1.18}_{-0.76}$
	$E_{\mathrm{abs1}}[\mathrm{keV}]$	$8.05^{+0.09}_{-0.07}$	$8.16^{+0.30}_{-0.23}$	$8.28^{+0.41}_{-0.38}$	$7.56^{+0.17}_{-0.16}$	$8.32^{+0.22}_{-0.24}$
	$\sigma_{\mathrm{abs1}}[\mathrm{keV}]$	<0.15	$0.31^{+0.38}_{-0.31}$	$0.93^{+0.40}_{-0.32}$	$0.31^{+0.17}_{-0.14}$	$0.48^{+0.27}_{-0.17}$
	$\mathrm{EW}_{\mathrm{abs1}}[\mathrm{eV}]$[b]	248^{+103}_{-104}	380^{+248}_{-298}	488^{+447}_{-451}	189^{+110}_{-106}	333^{+24}_{-25}
	$E_{\mathrm{abs2}}[\mathrm{keV}]$	$9.78^{+0.19}_{-0.18}$	$10.94^{+1.15}_{-0.73}$	$12.04^{+1.29}_{-3.10}$	$10.41^{+0.80}_{-0.70}$	$13.51^{+1.59}_{-0.73}$
	$\sigma_{\mathrm{abs2}}[\mathrm{keV}]$	$0.43^{+0.17}_{-0.15}$	$2.05^{+0.79}_{-0.53}$	$2.95^{+3.46}_{-1.51}$	$2.95^{+1.29}_{-0.74}$	$0.92^{+2.29}_{-0.92}$
	$\mathrm{EW}_{\mathrm{abs2}}[\mathrm{eV}]$[b]	461^{+104}_{-103}	1008^{+446}_{-707}	1643^{+506}_{-1146}	864^{+313}_{-340}	499^{+322}_{-320}
	χ^2/ν	106.1/103	121.8/114	121.0/104	179.0/142	64.9/69
	$P(\chi^2/\nu)$	0.40	0.29	0.17	0.02	0.62
7.......	Γ	$1.74^{+0.05}_{-0.06}$	$1.96^{+0.05}_{-0.06}$	$2.03^{+0.07}_{-0.06}$	$2.16^{+0.05}_{-0.04}$	$1.92^{+0.06}_{-0.06}$
	N_{H}	$4.7^{+1.9}_{-0.7}$	$20.7^{+6.9}_{-6.3}$	$5.80^{+0.08}_{-0.08}$	$13.32^{+3.83}_{-3.29}$	$11.5^{+5.4}_{-1.0}$
	ξ	<77	498^{+474}_{-321}	<0.22	228^{+84}_{-95}	<36
	$E_{\mathrm{abs1}}[\mathrm{keV}]$	$8.05^{+0.11}_{-0.06}$	$7.76^{+0.18}_{-0.17}$	$8.26^{+0.20}_{-0.13}$	$7.44^{+0.11}_{-0.10}$	$8.39^{+0.21}_{-0.76}$
	$\sigma_{\mathrm{abs1}}[\mathrm{keV}]$	<0.15	$0.37^{+0.26}_{-0.27}$	$0.95^{+0.41}_{-0.33}$	$0.27^{+0.12}_{-0.11}$	$0.37^{+0.54}_{-0.21}$
	$\mathrm{EW}_{\mathrm{abs1}}[\mathrm{eV}]$[b]	241^{+99}_{-88}	294^{+147}_{-175}	474^{+422}_{-451}	$231^{+0.22}_{-0.20}$	285^{+111}_{-127}
	$E_{\mathrm{abs2}}[\mathrm{keV}]$	$9.78^{+0.19}_{-0.18}$	$10.68^{+1.51}_{-3.91}$	$12.07^{+1.39}_{-4.38}$	$10.78^{+1.15}_{-4.38}$	$13.86^{+1.56}_{-0.66}$
	$\sigma_{\mathrm{abs2}}[\mathrm{keV}]$	$0.43^{+0.18}_{-0.17}$	$2.62^{+1.51}_{-1.21}$	$2.91^{+3.26}_{-1.49}$	$2.82^{+3.15}_{-1.52}$	$1.67^{+1.24}_{-0.88}$
	$\mathrm{EW}_{\mathrm{abs2}}[\mathrm{eV}]$[b]	455^{+187}_{-170}	963^{+519}_{-960}	1577^{+516}_{-1255}	1058^{+387}_{-550}	476^{+317}_{-318}

CHARTAS ET AL.

Table 2—*Continued*

Model[a]	Parameter[c]	Values Epoch 1[d]	Values Epoch 2[d]	Values Epoch 3[d]	Values Epoch 4[d]	Values Epoch 5[d]
	χ^2/ν	106.5/102	106.4/113	120.1/103	163.3/141	65.9/68
	$P(\chi^2/\nu)$	0.36	0.66	0.12	0.10	0.55

[a] Model 1 is a power-law with Galactic absorption and intrinsic absorption (APL; XSPEC model wabs*zwabs*pow); Model 2 is a power-law with Galactic absorption, intrinsic absorption, and a notch absorber (APL+No; XSPEC model wabs*zwabs*notch*pow); Model 3 is a power-law with Galactic absorption, intrinsic absorption, and a notch absorber (IAPL+No; XSPEC model wabs*absori*notch*pow); Model 4 is a power-law with Galactic absorption, intrinsic absorption, and an absorption edge (APL+Ed; XSPEC model wabs*zwabs*zedge*pow); Model 5 is a power-law with Galactic absorption, intrinsic ionized absorption, and an absorption edge (IAPL+Ed; XSPEC model wabs*absori*zedge*pow); Model 6 is a power-law with Galactic absorption, intrinsic absorption, and two absorption lines (APL+AL; XSPEC model wabs*zwabs*[pow+zgauss+zgauss]); Model 7 is a power-law with Galactic absorption, intrinsic ionized absorption, and two absorption lines (IAPL+2AL; XSPEC model wabs*absori*[pow+zgauss+zgauss]); All model fits include the Galactic absorption toward the source (Stark et al. 1992). $N_{\rm H}$ is the intrinsic column density expressed in units of 10^{22} atoms cm^{-2}. All fits have been performed on the combined spectrum of images A, B and C of APM 08279+5255.

[b] EW stands for equivalent width, which is defined as $EW = \int \frac{F_c - F_E}{F_c} dE$, where F_c is the continuous flux and F_E is the flux in the absorber.

[c] All absorption-line parameters are calculated for the rest frame.

[d] All errors are for 90% confidence unless mentioned otherwise with all parameters taken to be of interest except absolute normalization.

[e] $P(\chi^2/\nu)$ is the probability of exceeding χ^2 for ν degrees of freedom if the model is correct.

Table 3

Results from spectral fits using XSTAR to the *Chandra* and *XMM-Newton* observations of APM 08279+5255.

Model[a]	Parameter[c]	Values Epoch 1[d]	Values Epoch 2[d]	Values Epoch 3[d]	Values Epoch 4[d]	Values Epoch 5[d]
8........	Γ	$1.77^{+0.04}_{-0.04}$	$1.94^{+0.04}_{-0.04}$	$2.07^{+0.03}_{-0.02}$	$2.20^{+0.03}_{-0.03}$	$1.93^{+0.04}_{-0.04}$
	$N_{\rm H}$	$4.5^{+0.5}_{-0.3}$	$5.5^{+0.7}_{-0.2}$	$5.3^{+0.2}_{-0.3}$	$5.2^{+0.2}_{-0.4}$	$10.5^{+1.1}_{-3.9}$
	$N_{\rm Habs1}$	100	17 ± 2	39	$12^{+2.0}_{-3}$	$8.5^{+3.8}_{-3.5}$
	$\log\xi_{\rm abs1}$	$4.0^{+0.08}_{-0.1}$	$3.1^{+0.12}_{-0.7}$	$3.6^{+0.9}_{-0.3}$	$3.1^{+0.05}_{-0.17}$	$3.3^{+0.7}_{-0.6}$
	$z_{\rm abs1}$	3.2 ± 0.10	3.0 ± 0.1	3.1 ± 0.1	3.3 ± 0.1	2.94 ± 0.10
	$N_{\rm Habs2}$	10^{+8}_{-5}	14^{+4}_{-8}	83	10^{+2}_{-2}	40^{+40}_{-32}
	$\log\xi_{\rm abs2}$	$3.2^{+0.2}_{-0.3}$	$3.5^{+0.7}_{-0.4}$	$3.9^{+0.2}_{-0.3}$	$3.1^{+0.13}_{-0.05}$	$3.9^{+0.5}_{-0.5}$
	$z_{\rm abs2}$	2.4 ± 0.1	2.0 ± 0.1	1.7 ± 0.1	2.3 ± 0.1	1.48 ± 0.07
	χ^2/ν	114.3/103	118.3/116	129.2/104	167.2/142	71.5/69
	$P(\chi^2/\nu)$	0.21	0.42	0.05	0.07	0.40
9........	Γ	$1.79^{+0.03}_{-0.04}$	$1.96^{+0.05}_{-0.10}$	$2.08^{+0.03}_{-0.03}$	$2.32^{+0.1}_{-0.09}$	$1.93^{+0.03}_{-0.04}$
	$N_{\rm H}$	$4.4^{+0.5}_{-0.5}$	$5.7^{+0.3}_{-0.8}$	$5.2^{+0.20}_{-0.23}$	$5.5^{+0.4}_{-0.3}$	$10.5^{+1.0}_{-1.2}$
	$K_{\rm direct}$	$<1\times10^{-5}$	$2.9^{+1.0}_{-2.2}\times10^{-5}$	$1.2^{+4.9}_{-1.2}\times10^{-5}$	$1.4^{+0.2}_{-0.2}\times10^{-4}$	$<5\times10^{-5}$
	$N_{\rm Habs1}$	100	50	100	72^{+30}_{-22}	18^{+36}_{-12}
	$\log\xi_{\rm abs1}$	$3.8^{+0.07}_{-0.3}$	$3.1^{+0.14}_{-0.07}$	$3.3^{+0.06}_{-0.05}$	$3.0^{+0.07}_{-0.07}$	$3.3^{+0.5}_{-0.7}$
	$z_{\rm abs1}$	3.2 ± 0.1	3.0	3.04 ± 0.1	3.2 ± 0.1	2.95 ± 0.1
	$K_{\rm abs1}$	$8^{+2}_{-1}\times10^{-5}$	$7.8^{+1.6}_{-1.7}\times10^{-5}$	$5.8^{+0.6}_{-0.7}\times10^{-5}$	$1.2^{+0.3}_{-0.2}\times10^{-4}$	$1.1^{+3.2}_{-0.4}\times10^{-4}$
	$N_{\rm Habs2}$	22	50^{+12}_{-7}	100	100	100
	$\log\xi_{\rm abs2}$	$3.0^{+0.4}_{-0.3}$	$3.5^{+0.6}_{-0.6}$	$4.0^{+0.08}_{-0.3}$	$3.1^{+0.3}_{-0.2}$	$3.8^{+0.2}_{-0.9}$
	$z_{\rm abs2}$	2.3 ± 0.1	2.0	1.6 ± 0.1	2.3 ± 0.1	1.5 ± 0.1
	$K_{\rm abs2}$	$5^{+2}_{-1}\times10^{-5}$	$5^{+1.6}_{-1.2}\times10^{-5}$	$1.2^{+0.2}_{-0.2}\times10^{-4}$	$0.8^{+0.4}_{-0.3}\times10^{-4}$	$6.3^{+2.5}_{-0.3}\times10^{-4}$
	χ^2/ν	116.9/101	116.2/114	116.2/102	156./140	71.7/67
	$P(\chi^2/\nu)$	0.13	0.43	0.16	0.17	0.33

[a] Model 8 is a power-law with Galactic absorption, intrinsic neutral absorption, and two intrinsic ionized absorbers (APL + 2IA; XSPEC model wabs*zwabs*warmabs*warmabs(pow)). Model 9 is a power-law with Galactic absorption, intrinsic neutral absorption, and two partially covered intrinsic ionized absorbers (APL + PC*(2IA); XSPEC model wabs*zwabs*(pow + warmabs*pow + warmabs*pow)). In the APL + PC*(2IA) model $K_{\rm direct}$, $K_{\rm abs1}$ and $K_{\rm abs2}$ are the photon flux densities (photons keV^{-1} cm^{-2} s^{-1}) at 1 keV of the one non-absorbed and two absorbed components, respectively. All model fits include the Galactic absorption toward the source (Stark et al. 1992). All fits have been performed on the combined spectrum of images A, B and C of APM 08279+5255. $N_{\rm H}$ is the intrinsic column density expressed in units of 10^{22} atoms cm^{-2}. We note that in several cases (especially for spectral fits using model 9) the value of the column density of the ionized absorber reaches the maximum allowable value in our XSTAR model of 1×10^{24} atoms cm^{-2}. The errors for several parameters are not listed because the fits in these cases could not provide any useful constraints. All listed errors are at the 68% confidence level.

CHARTAS ET AL.

TABLE 4

PROJECTED MAXIMUM OUTFLOW VELOCITIES, MASS-OUTFLOW RATES AND EFFICIENCIES OF OUTFLOWS IN APM 08279+5255 [a].

Epoch	Instr.	v_{abs1} [c]	log N_H(abs1)	$\dot{M}$ (abs1) [$M_\odot \mu_L^{-1} yr^{-1}$]	ϵ_K (abs1)	v_{abs2} [c]	log N_H(abs2)	$\dot{M}$ (abs2) [$M_\odot \mu_L^{-1} yr^{-1}$]	ϵ_K (abs2)
1	ACIS S3	$0.18^{+0.01}_{-0.01}$	22.9 ± 0.4	393^{+403}_{-276}	$0.014^{+0.014}_{-0.01}$	$0.36^{+0.02}_{-0.02}$	23.1 ± 0.5	1229^{+1098}_{-792}	$0.17^{+0.15}_{-0.11}$
2	EPIC pn	$0.20^{+0.03}_{-0.04}$	23.1 ± 0.3	656^{+846}_{-480}	$0.026^{+0.034}_{-0.019}$	$0.46^{+0.08}_{-0.06}$	23.4 ± 0.3	3141^{+899}_{-2246}	$0.68^{+0.20}_{-0.49}$
3	EPIC pn	$0.21^{+0.05}_{-0.05}$	23.2 ± 0.3	891^{+1288}_{-651}	$0.04^{+0.06}_{-0.03}$	$0.53^{+0.07}_{-0.25}$	23.6 ± 0.3	5508^{+6437}_{-3973}	$1.61^{+1.89}_{-1.16}$
4	EPIC pn	$0.12^{+0.02}_{-0.02}$	22.8 ± 0.3	209^{+250}_{-158}	$0.003^{+0.004}_{-0.002}$	$0.41^{+0.06}_{-0.06}$	23.4 ± 0.4	2549^{+2593}_{-1719}	$0.46^{+0.47}_{-0.31}$
5	ACIS S3	$0.21^{+0.03}_{-0.03}$	23.0 ± 0.7	609^{+542}_{-396}	$0.03^{+0.03}_{-0.02}$	$0.61^{+0.07}_{-0.04}$	23.0 ± 0.3	1593^{+1916}_{-1165}	$0.62^{+0.74}_{-0.45}$

[a]The estimated values of the outflow properties were based on fits that assumed an absorbed power-law model with two absorption lines. The values of $\dot{M}$ and ϵ_K are obtained by equations 1 and 2, respectively, assuming $M_{BH} \sim 10^{12} \mu_L^{-1} M_\odot$ (see §3.2) and $L_{bol} = 7 \times 10^{15} \mu_L^{-1} L_\odot$ (Irwin et al. 1998; Reichers et al. 2009).

TABLE 5

THE MINIMUM AND MAXIMUM ENERGIES AND VELOCITIES OF THE HIGH-ENERGY ABSORPTION FEATURES IN APM 08279+5255.

Epoch	Instrument	$E_{\min}$ [keV]	$E_{\max}$ [keV]	$v_{\min}$ [c]	$v_{\max}$ [c]
1	ACIS S3	8.05±0.17	10.64±0.27	0.18±0.02	0.43±0.02
2	EPIC pn	7.54±0.74	15.04±1.22	0.12±0.09	0.67±0.04
3	EPIC pn	6.42±0.82	17.94±2.96	0.04±0.04	0.76±0.07
4	EPIC pn	6.94±0.35	16.31±1.17	0.04±0.04	0.71±0.04
5	ACIS S3	7.36±0.56	15.35±2.12	0.09±0.07	0.68±0.07

[a]$E_{\min}$ and $E_{\max}$ are estimated from spectral fits using model 6 of Table 2.

CHARTAS ET AL.
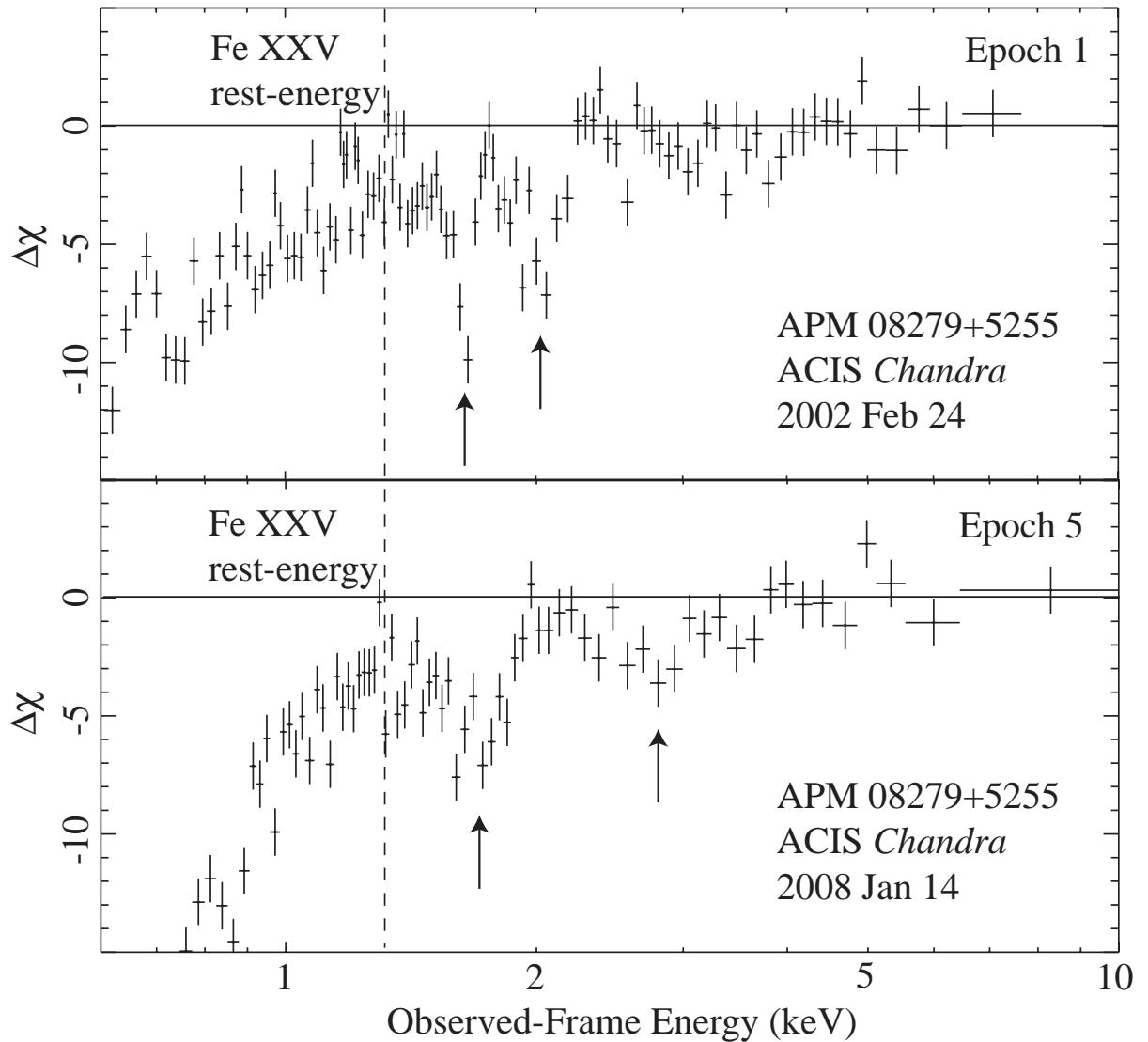
FIG. 1.— $\Delta\chi$ residuals between the best-fit Galactic absorption and power-law model and the *Chandra* ACIS spectra of APM 08279+5255. This model is fit to events with energies lying within the ranges 4.5–10 keV. The arrows indicate the best-fit energies of the absorption lines of the first and second outflow components for epoch 1 (top panel) and epoch 5 (lower panel) obtained in fits that used model 6 of Table 2.
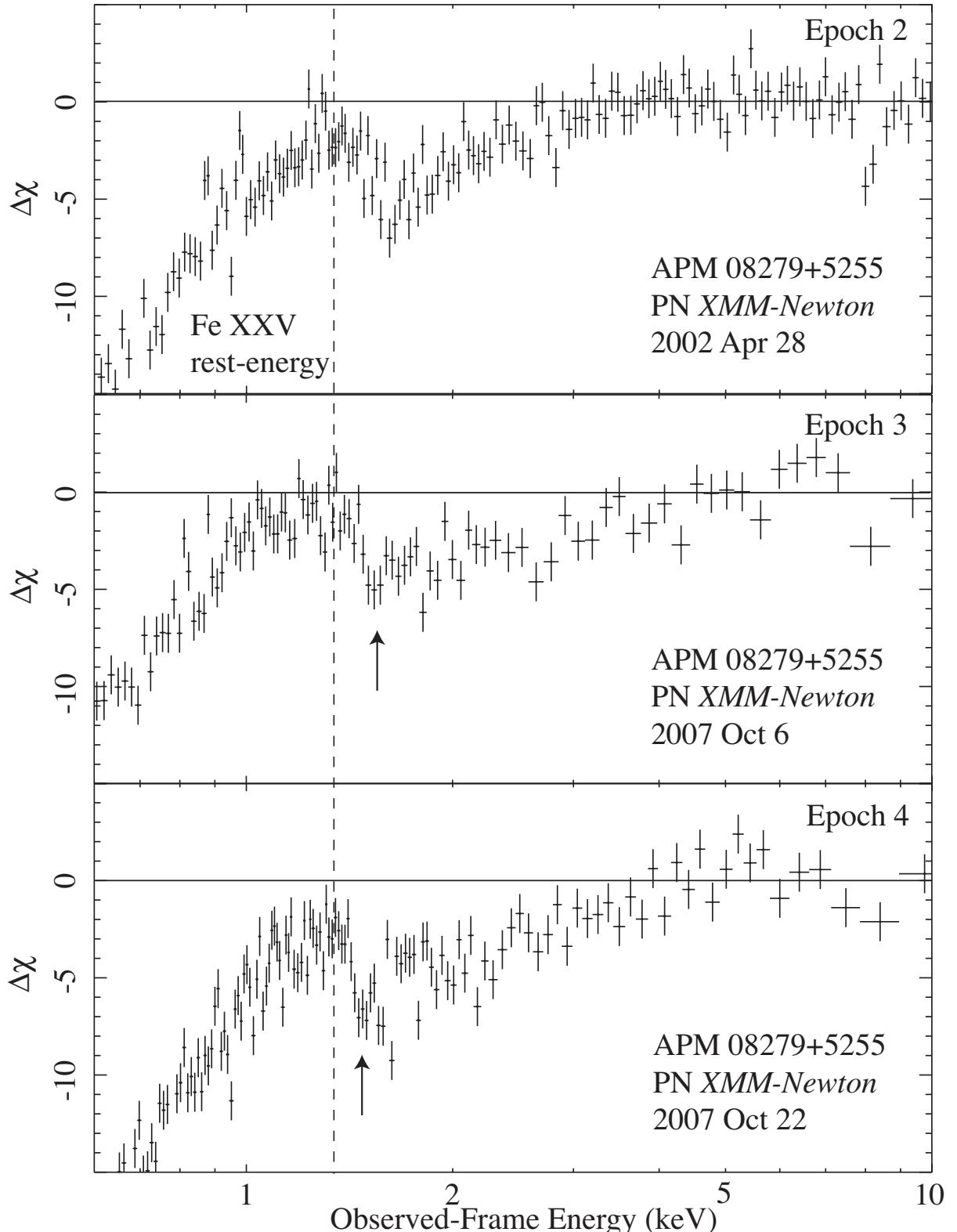
FIG. 2.— $\Delta\chi$ residuals between the best-fit Galactic absorption and power-law model and the *XMM-Newton* pn spectra of APM 08279+5255. This model is fit to events with energies lying within the range 4.5–10 keV. The arrows indicate the best-fit energies of the absorption line of the first outflow component for epoch 3 (middle panel) and epoch 4 (bottom panel) obtained in fits that used model 6 of Table 2.
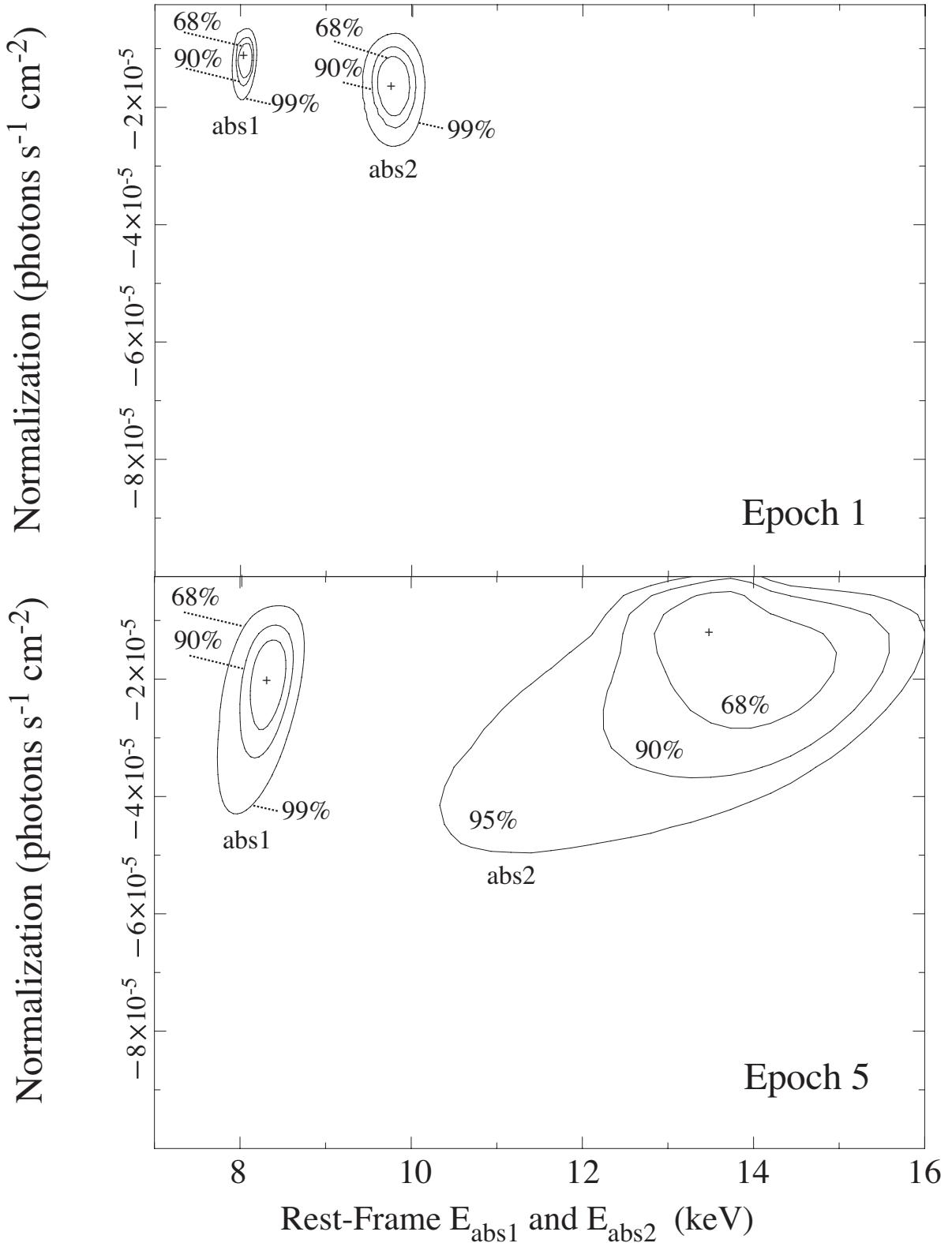
FIG. 3.— 68%, 90%, and 99% confidence contours between the normalizations of the absorption lines at E_{abs1} and E_{abs2} and the respective energies E_{abs1} and E_{abs2} for the *Chandra* 2002 (top panel) and *Chandra* 2008 (bottom panel) observations of APM 08279+5255 assuming fit 6 of Table 2. The 99% confidence contour of component *abs*2 for epoch 5 is not well constrained and the 95% contour is shown instead.
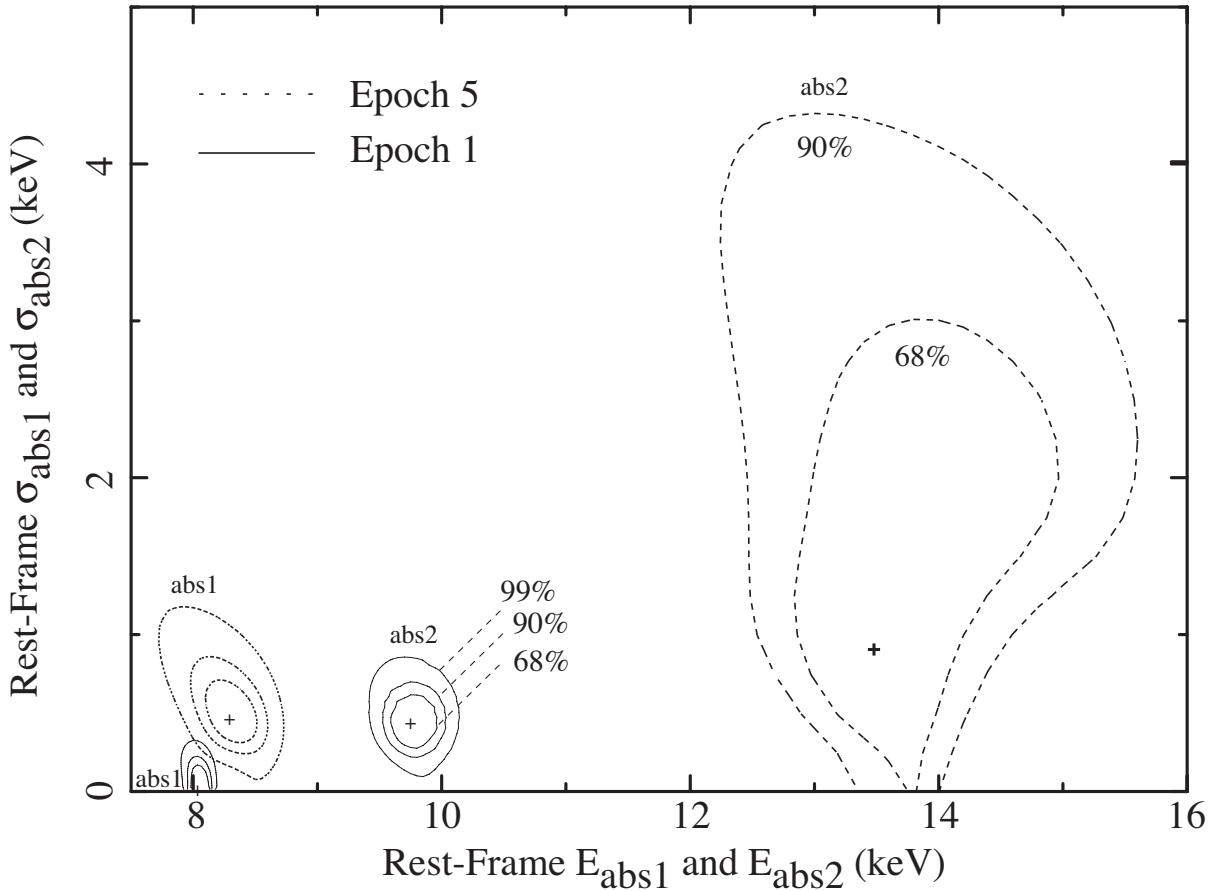
FIG. 4.— 68%, 90% and 99% confidence contours between best-fit energies E_{abs1} and E_{abs2} and energy widths σ_{abs1} and σ_{abs2} of the absorption lines for the *Chandra* 2002 (Epoch 1) and *Chandra* 2008 (Epoch 5) observations of APM 08279+5255 assuming fit 6 of Table 2. The 99% confidence contour of component *abs2* for epoch 5 is not well constrained and not shown in this plot.

CHARTAS ET AL.
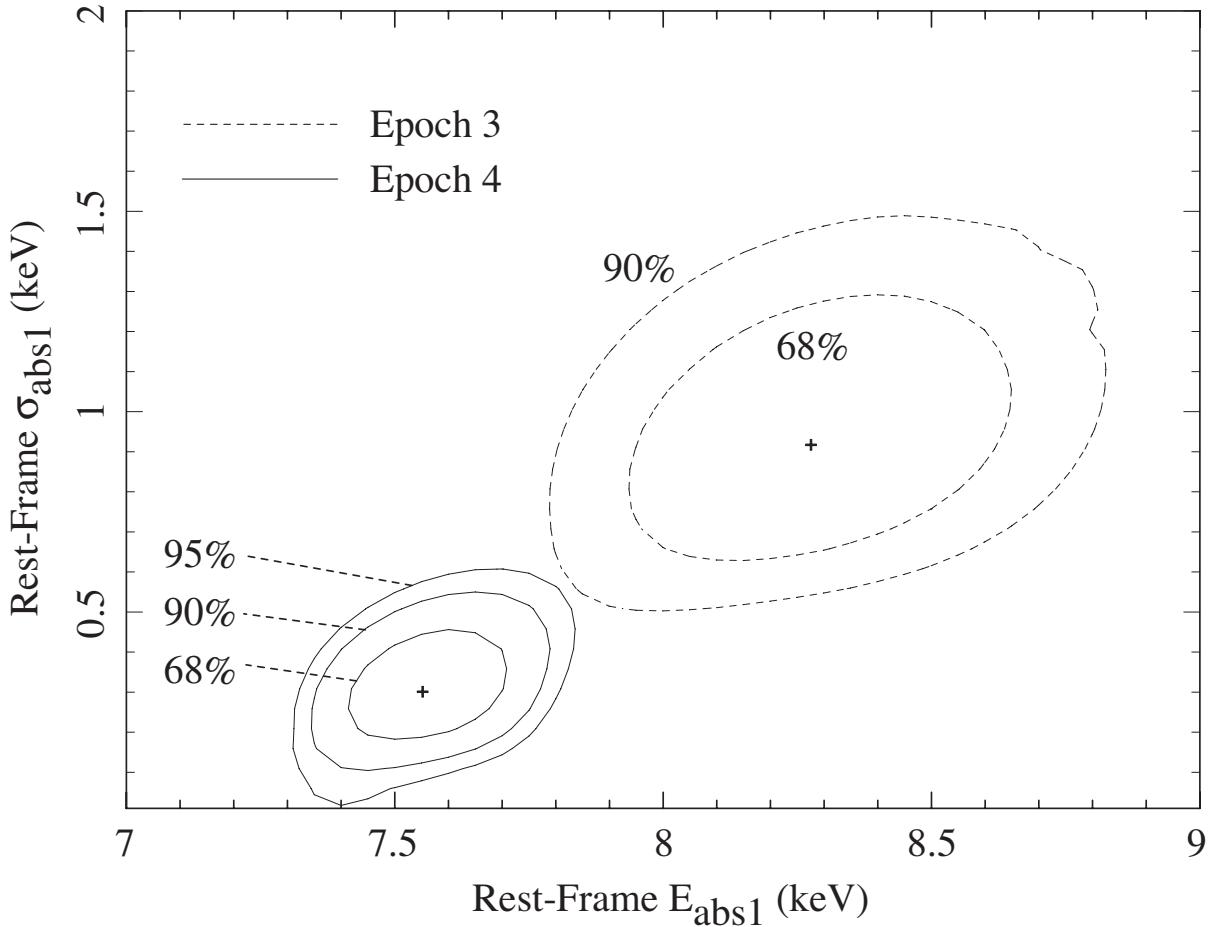
FIG. 5.— 68%, 90% and 95% χ^2 confidence contours of E_{abs} versus σ_{abs} of the first absorption line in epoch 3 (dotted line) and epoch 4 (solid line) assuming the APL + 2 AL model (see model 6 of Table 2). The 95% confidence contour for epoch 3 is not well constrained and not shown in this plot.
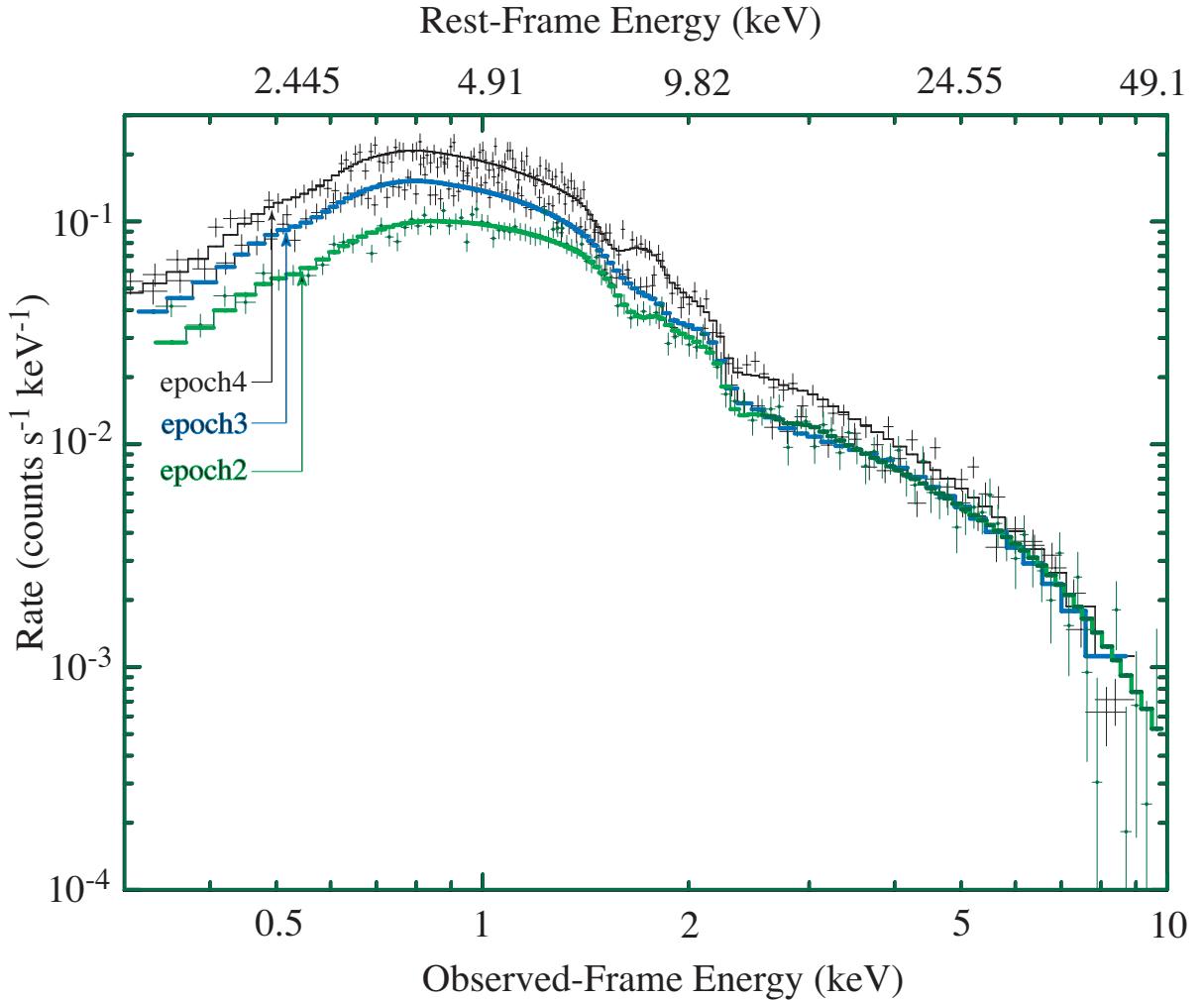
FIG. 6.— The spectra and best-fit models (model 6 of Table 2) of the *XMM-Newton* observations of APM 08279+5255. We note the significant variability of the X-ray BALs (extending between ≈ 1.5–3.6 keV) and continuum between epochs 3 and 4 that are separated by only ∼ 3.3 days (proper-time).
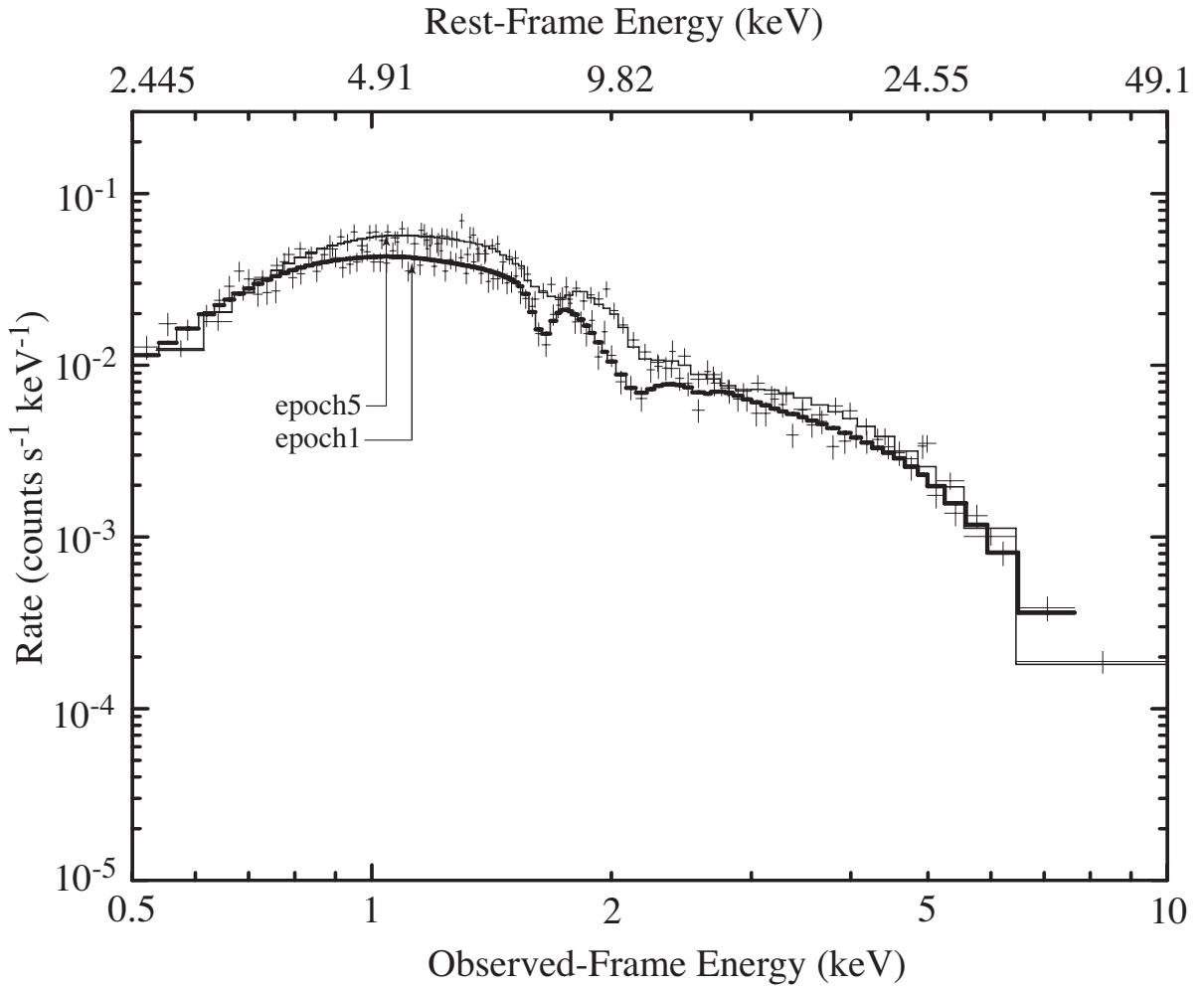
FIG. 7.— The spectra and best-fit models (model 6 of Table 2) of the *Chandra* observations of APM 08279+5255. We note the significant variability of the X-ray BALs extending between ≈ 1.5–3.6 keV.
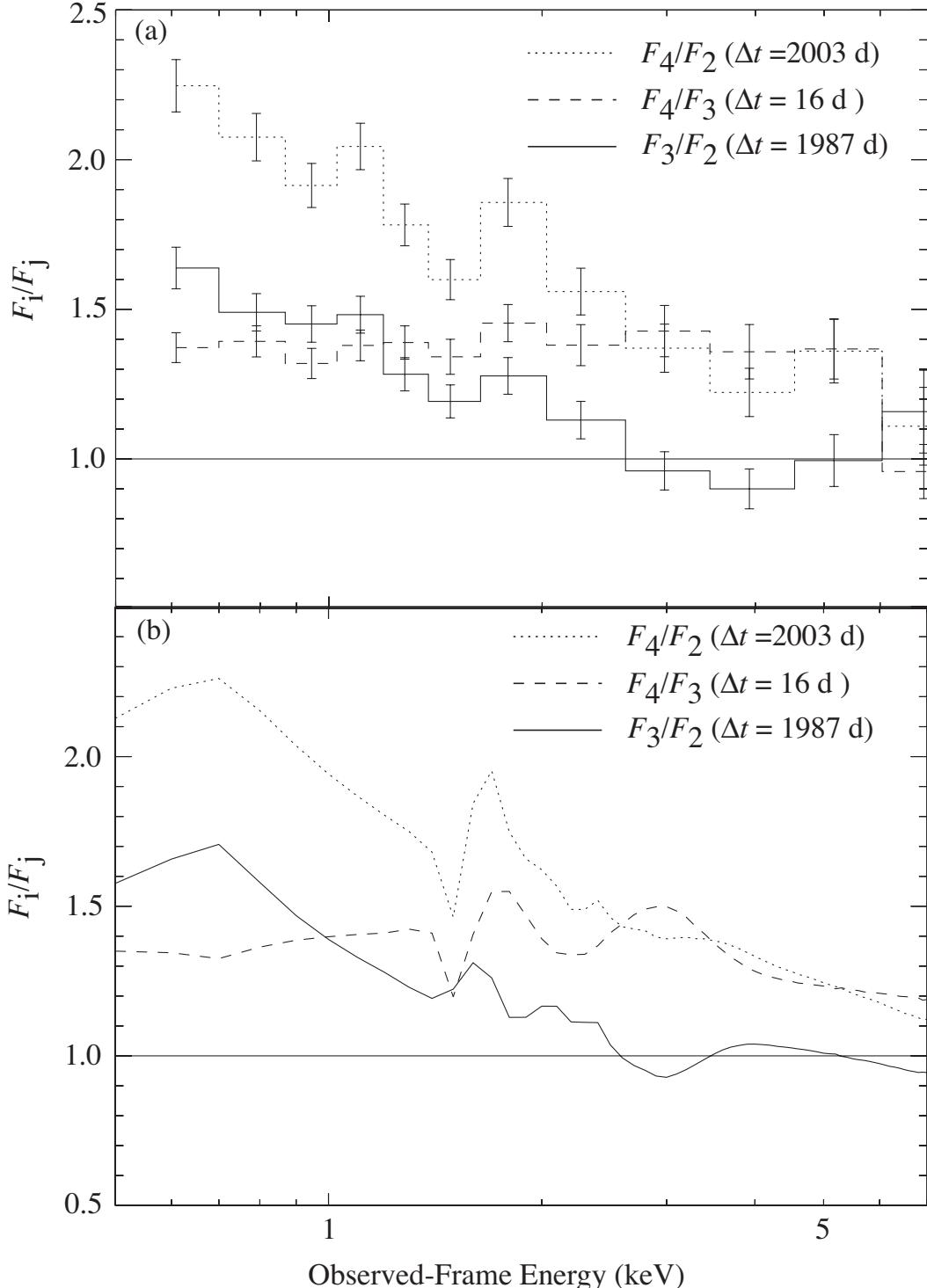
FIG. 8.— The ratios of the (a) observed and (b) best-fit-modeled (using model 6 of Table 2) flux densities F_i/F_j between the three *XMM-Newton* observations of APM 08279+5255 listed in Table 1, where i and j represent the epochs compared, Δt is the observed-frame time between epochs and F is the flux density in units of counts s^{-1} keV^{-1}. Note that a significant change of flux density is observed between all observations over the entire spectrum of APM 08279+5255. The spectral change between epochs 3 and 4 is particularly remarkable since it occurs over a period of only ~ 3.3 days (proper-time) implying a size-scale of $\sim 7.4 \times 10^{15}$ cm which is comparable to $r_{\mathrm{ISCO}} = 4.5 \times 10^{15}$ cm for the case of a Schwarzschild black hole in APM 08279+5255.
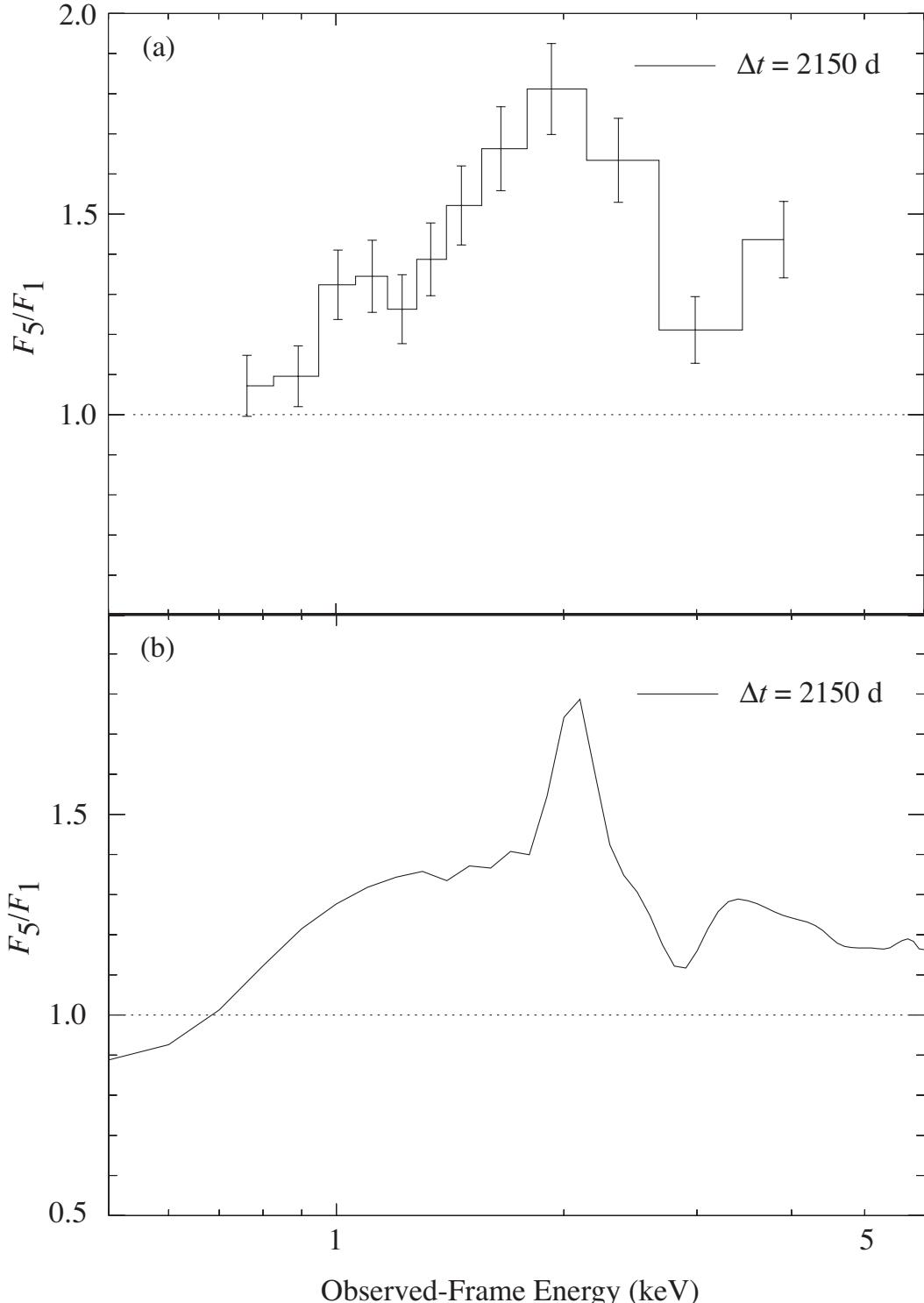
Fig. 9.— The ratios of the (a) observed and (b) best-fit-modeled (using model 6 of Table 2) flux densities F_5/F_1 between the two *Chandra* observations of APM 08279+5255 listed in Table 1, where F_1 and F_5 are the flux densities for epochs 1 and 5 respectively. Δt is the observed-frame time between epochs. Note that a significant change of flux density is observed near the region of the Fe BALs ($\sim$ 1.5–3.6 keV).
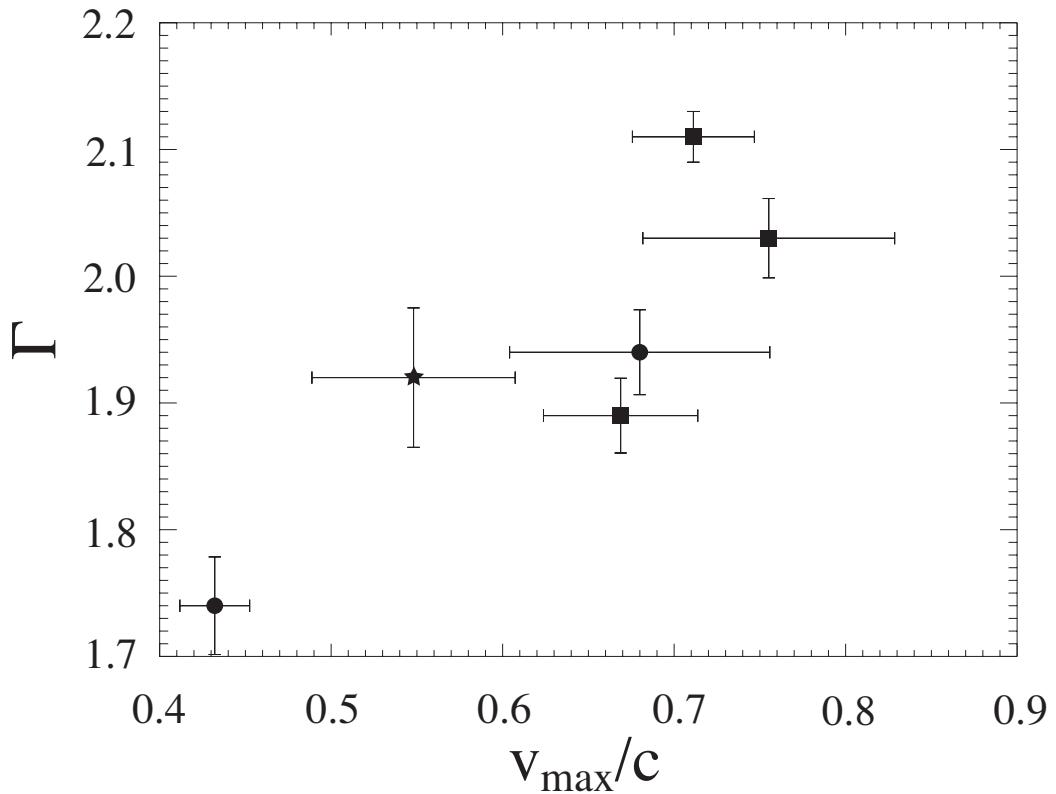
FIG. 10.— Maximum outflow velocity, v_{max}, observed from APM 08279+5255 as a function of the X-ray photon index, Γ. v_{max} and Γ were derived from fits to the spectra of APM 08279+5255 with a model that included an absorbed power-law and two Gaussian absorption lines (model 6 of Table 2). Errors shown are at the 68% confidence level. Data shown with circles, a star, and squares are obtained from *Chandra*, *Suzaku* and *XMM-Newton* observations respectively.
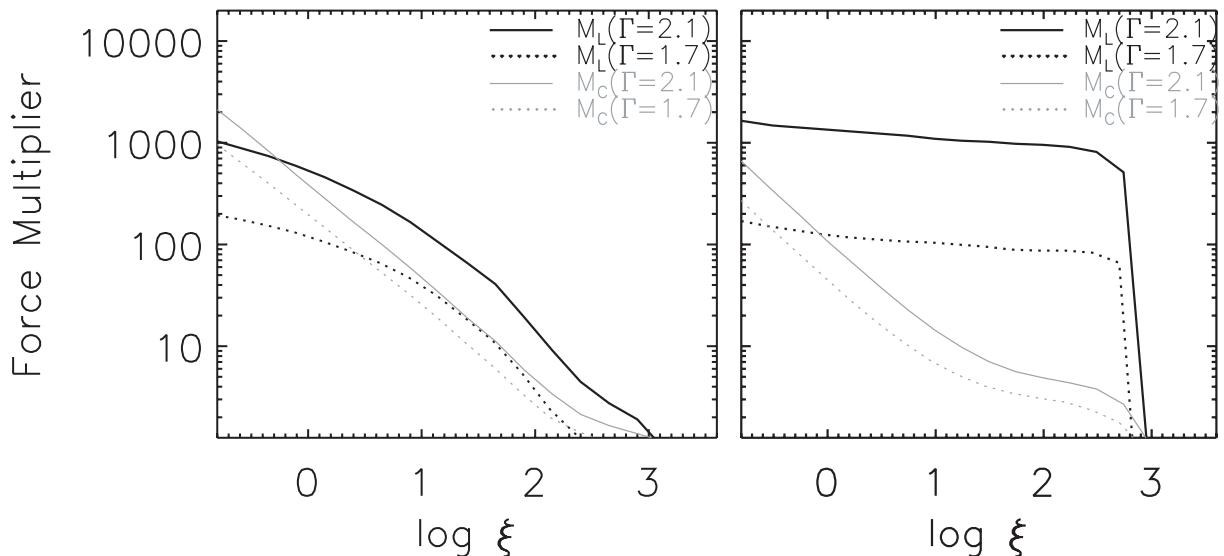
FIG. 11.— The bound-free, M_C, and bound-bound, M_L, components of the force multiplier are shown as a function of the ionization parameter. Force multipliers are calculated for SEDs with photon indices of $\Gamma = 2.1$ (solid lines) and $\Gamma = 1.7$ (dotted lines). In the left panel we have assumed no absorbing shield, whereas, in the right panel the soft and hard SEDs have been attenuated by an absorber with $\log N_H = 22.8$.
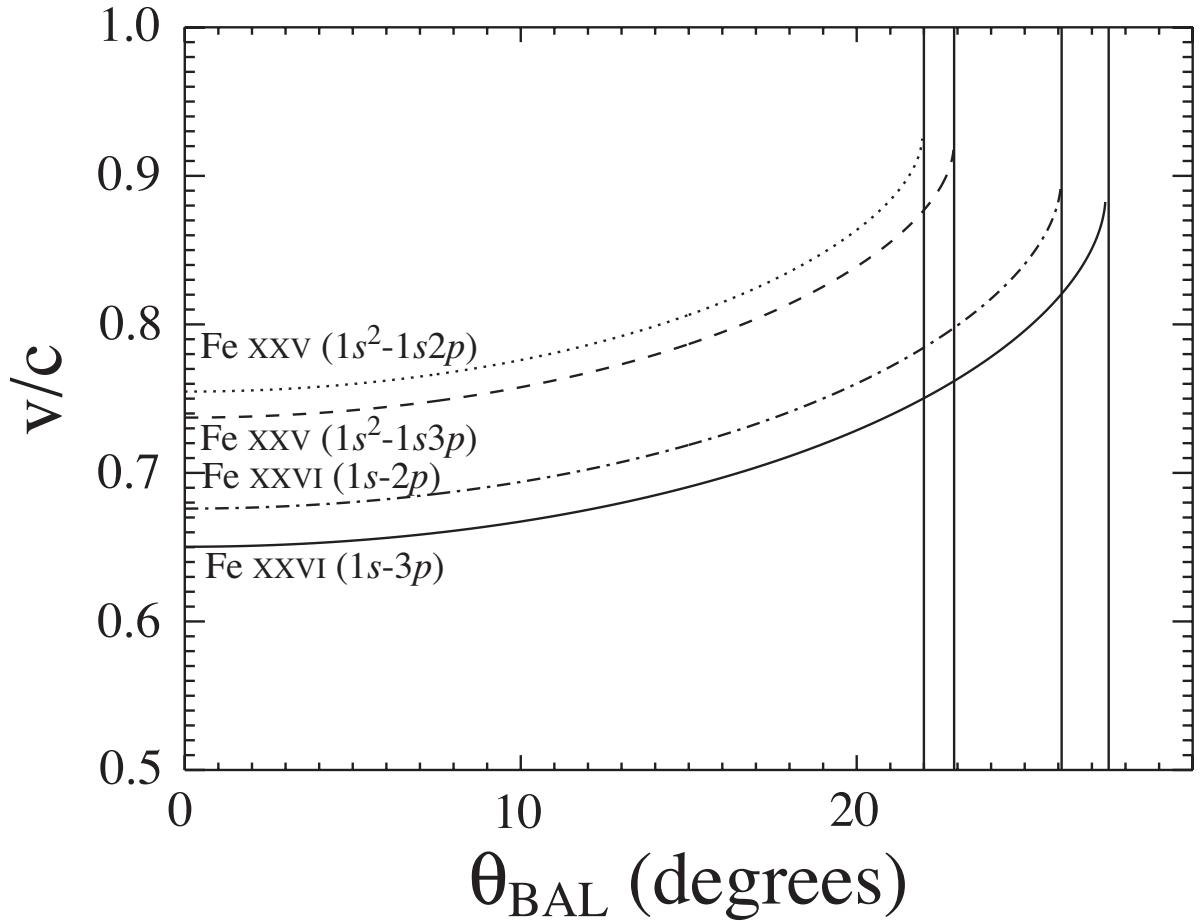
FIG. 12.— Maximum outflow velocity as a function of the angle between the outflow direction and our line of sight. Shown are the outflow velocities for the most likely resonance transitions responsible for the observed X-ray BALs in APM 08279+5255. The outflow velocities were calculated using the relativistic Doppler formula for the case of the maximum rest-frame energy of the X-ray BALs of $E_{max} = 17.9$ keV (see Table 5) observed in epoch 3.